AN ABSTRACT OF THE THESIS OF

Meghan M. Dalton for the degree of Master of Science in Atmospheric Sciences presented on September 7, 2011

Title: Comparison of radiative feedback variability over multiple time scales in climate model and reanalysis data

Abstract approved:

Karen M. Shell

In a steady state, the Earth's absorbed solar radiation (ASR) balances the outgoing longwave radiation (OLR) at the top of the atmosphere (TOA). In response to a radiative forcing, that is, an external perturbation to the top of the atmosphere energy balance, the Earth's climate system adjusts until reaching a new state of radiative equilibrium. For example, an increased amount of carbon dioxide in the atmosphere will absorb more terrestrial radiation thus decreasing the amount of outgoing longwave radiation at the top of the atmosphere. Since more energy is kept in the system, the global temperature rises, and the Earth emits more radiation until the OLR is in equilibrium with the incoming solar radiation. The magnitude of the climate response to an imposed forcing is dependent upon the strength of physical climate feedbacks within the system (i.e., water vapor, temperature, surface albedo, and clouds) which act to amplify or dampen the response. Global climate models project that the Earth's climate, represented by the globally averaged surface temperature, will warm between 2.0-4.5 Kelvin if we double the concentration of carbon dioxide in the atmosphere (Soloman et al., 2007). The differences in global climate model simulations of the climate response to an imposed forcing are largely due to differences in climate feedback strengths among individual models (Soloman et al., 2007).

This thesis assesses how well short-term feedback variability relates to long-term feedbacks with the goal of using an observational dataset to ultimately constrain long-term feedback estimates. First, feedbacks and feedback variability are quantified on three time scales over two time periods in the 20th century as simulated by 13 global climate models. The three time scales are: annual, interannual, and decadal. These time scales are characterized, respectively, by the amplitude of the seasonal cycle, standard deviation of TOA flux anomalies, and least-squares linear trend of TOA flux anomalies. Second, time scales of feedback variability are compared over the two time periods. The two time periods

are: 20-years (short-term) and 100-years (long-term). Third, modeled short-term feedback variability is compared with the European Center for Medium-range Weather Forecasts ERA-Interim reanalysis observational data product. The method used to quantify individual climate feedbacks in models is the radiative kernel technique (Soden et al., 2008). This technique decomposes each feedback into two components: the TOA flux change due to a standard change in the feedback variable (radiative kernel), and the change in the feedback variable due to a particular climate forcing (climate response). The radiative kernel technique can also be used effectively to analyze climate feedbacks in reanalysis datasets. Monthly departures from the mean of each feedback variable (specific humidity, atmospheric temperature, and surface albedo), at each grid point and vertical level, are multiplied by the corresponding radiative kernel (Shell et al., 2008) to obtain TOA radiative flux anomalies due to each variable.

The annual cycle provides a better constraint than interannual or decadal variability on global and hemispheric long-term feedbacks. For water vapor and atmospheric temperature, this result is strong for both the northern and southern hemispheres. For surface albedo, the strongest relationship between the annual cycle and long-term feedback occurs in the southern hemisphere. However, using the annual cycle to estimate the long-term feedback still results in a large uncertainty. For atmospheric temperature and water vapor, the reanalysis observations of the annual cycle are within the range of models, but for surface albedo, the reanalysis annual cycle is smaller in magnitude than all models. Understanding the differences between modeled and observed annual, interannual, and decadal variability of climate feedbacks and corresponding TOA flux anomalies and how they relate to climate sensitivity will help reduce the uncertainty associated with future climate projections.

Comparison of radiative feedback variability over multiple time scales in climate model and reanalysis data

by
Meghan M. Dalton

A THESIS

submitted to

Oregon State University

in partial fulfillment of
the requirements for the
degree of

Master of Science

Presented September 7, 2011
Commencement June 2012

Master of Science thesis of Meghan M. Dalton presented on September 7, 2011.

APPROVED:

Major Professor, representing Atmospheric Sciences

Dean of the College of Oceanic and Atmospheric Sciences

Dean of the Graduate School

I understand that my thesis will become part of the permanent collection of Oregon State University libraries. My signature below authorizes release of my thesis to any reader upon request.

Meghan M. Dalton, Author

TABLE OF CONTENTS

TABLE OF CONTENTS (continued)

LIST OF FIGURES

LIST OF FIGURES (continued)

LIST OF TABLES

Comparison of Radiative Feedback Variability Over Multiple Time Scales in Climate Model and Reanalysis Data

Chapter 1

Introduction

Evidence for the current warming of the global climate is unequivocal according to the Fourth Assessment Report of the Intergovernmental Panel on Climate Change (IPCC) (IPCC, 2007). The IPCC also concludes that it is "very likely" that the observed warming is not fully explained by natural climate variability alone and includes contributions from mankind (i.e., increasing concentrations of carbon dioxide (CO_2) and other greenhouse gases in the atmosphere). The additional atmospheric concentrations of greenhouse gases force the climate to warm by absorbing and retaining more of the energy radiated by the Earth that would otherwise escape to space. Even if human civilization ceased to emit carbon dioxide and other greenhouse gases, the climate would continue to warm over the next century. The ability to accurately project how much the Earth will warm in the future is important for planning adaptive resource management strategies for a changing future climate. How much the Earth will warm in the coming century depends on the magnitude of future CO_2 emissions, the rate at which the ocean takes up heat, and the sensitivity of the climate to alterations of the balance of energy entering and exiting the Earth system through the top of the atmosphere.

In a steady state, the Earth's temperature is unchanging, and thus the energy entering the Earth system balances the energy exiting the Earth system. The energy entering the Earth comes in the form of solar radiation (sunlight). Some incoming solar radiation is reflected by the Earth's atmosphere and surface back out to space. That which is not reflected, the absorbed solar radiation (ASR), is absorbed by the Earth's surface and to a lesser extent, by the atmosphere. The Earth's surface radiates longwave (infrared) energy according to its temperature and emissivity, and much of that energy is absorbed by gases and clouds in the atmosphere. The atmosphere also radiates longwave energy in all directions. The net result of the atmosphere's

effect is to absorb more upwelling longwave energy than it emits, resulting in outgoing longwave radiation (OLR) at the top of the atmosphere (TOA) that is less than the longwave radiation emitted by the Earth's surface. On a global and time averaged domain, the ASR and OLR roughly balance each other, but at a given time the incoming and outgoing energy may not exactly balance and tend to fluctuate around a steady state. The recent alteration of the composition of the atmosphere, that of increased concentrations of carbon dioxide and other gases that selectively absorbed longwave radiation (i.e. greenhouse gases), has forced the climate system out of steady state such that on average the amount of energy absorbed by the system is greater than the energy escaping the system (Trenberth et al., 2009) leading to a rise in the global average surface temperature.

Because atmospheric CO_2 is a gas that selectively absorbs infrared (or longwave) radiation emitted by the Earth, higher concentrations of CO_2 in the atmosphere will absorb more longwave energy, resulting in a warmer Earth. The climate sensitivity is how much the Earth will warm given this retention of energy. The sensitivity of the climate depends on the strength of internal climate processes that affect the top of the atmosphere radiative energy flows. These internal processes are known as radiative feedbacks. The radiative feedbacks include those due to surface albedo, water vapor, temperature, and clouds.

The temperature feedback is technically the response of the climate system to a retention of radiative energy, but the temperature response influences the TOA energy balance and thus the climate sensitivity. The TOA influence of temperature changes is the most negative (dampening) feedback in the climate system. A warmer Earth emits more longwave radiation according the Stefan-Boltzmann emission (emission $= \sigma T^4$) leading to an increase in the outgoing longwave radiation at the top of the atmosphere. This is a regulating cooling effect. When the surface air temperature of the Earth increases, other components of the climate system are affected, which in turn affect the global energy balance of the Earth and feedback to either amplify or dampen the initial climate response. For example, as temperatures rise, snow and ice melt in the high latitude regions. Since ice is more reflective than the land or ocean beneath it, the Earth's surface now absorbs more solar radiation. This is an amplifying warming effect. Warmer temperatures also increase the saturation specific humidity of air and allow the atmosphere to hold more water vapor. Water vapor is a selective absorber of longwave radiation (i.e. greenhouse gas) so the amount of longwave radiation emitted to space is now less. Again, this is an amplifying warming

effect. Changes in cloud properties also affect the energy balance because clouds both absorb longwave radiation and reflect shortwave radiation. The sign of cloud changes is uncertain and varies spatially and seasonally. To restore the climate system to a state of equilibrium, the cumulative effect of all these changes must be to eventually reach a balance between the incoming and outgoing energy.

The equilibrium climate sensitivity (ECS) is defined as the resulting temperature change after the climate system has equilibrated to an instantaneous doubling of atmospheric CO_2 concentrations. The actual equilibrium climate sensitivity of the Earth is unknown. Estimates of the ECS are generally obtained using an ensemble of Atmospheric Global Climate Models (AGCMs). AGCMs consist of a dynamical atmospheric model coupled to a slab-ocean model. The current range of ECS among AGCMs used in the Fourth Assessment Report (AR4) of the IPCC is 2.1 to 4.4 K with a most likely value of ≈ 3.2 K (Randall et al., 2007). While climate models have improved since the Third Assessment Report of the IPCC, the range in ECS has not narrowed much. This spread in ECS among climate models is due to the uncertainty in the climate sensitivity components, that is, radiative feedbacks among models. The largest contributor to the spread in climate sensitivity is clouds, followed by water vapor and lapse rate, then surface albedo (Colman, 2003a). Satellite observations of radiation flows are used to estimate climate sensitivity, but since the Earth is not in equilibrium, an "effective climate sensitivity" is being inferred. Assuming constant feedback strengths, the effective climate sensitivity computed at a given time within a transient climate state is an estimate of the ECS (Randall et al., 2007). When the Earth system is in a transient state, the rate at which the ocean takes up heat will partly determine the overall sensitivity. Coupled Atmosphere-Ocean Global Climate Models (AOGCMs), with a dynamic ocean model with multiple depth layers, are used to calculate effective climate sensitivities from transient simulations of the climate.

There are two ways in which to study the Earth's climate and climate changes: through the lens of observational instrumentation including satellites, ground measurements, and proxies (past and present), and through the careful use of global climate models (past, present, and future). In terms of the Earth's energy balance, there are only a couple of decades of observations from which information about the short-term variability of TOA radiative fluxes can be gleaned. An open question is to what extent any long-term climate change information is contained in annual, interannual and decadal variability of TOA flux anomalies derived from a short record. Climate models can be useful in this situation because there are many realizations

of past, present, and future climates. It is therefore useful to study the relationship between short-term and long-term variability of TOA flux anomalies with climate models. To this end, the work of this thesis characterizes the short-term and long-term variability of TOA flux anomalies of 20^{th} century simulations from 13 AOGCMs used in the AR4 of the IPCC.

The purpose of this work is to study the variability of global and hemispheric TOA effects due to the variability in the feedback variables: water vapor, temperature, and surface albedo, in order to understand any relationships between this variability on different time scales. If any information about long-term changes is contained in annual or interannual variability of TOA flux anomalies, then observational validation of the short-term variability may be able to constrain variability or changes over a longer period. This thesis considers the following questions: what is the nature of variability of TOA effects of feedback variables between short and long time scales in climate models and how does short-term variability in climate models compare with an observational dataset?

Many study short-term feedbacks in models and attempt to relate short-term feedbacks on the annual to interannual time scales to long term feedbacks on the century time scale (e.g. Hall and Qu, 2006; Knutti et al., 2006). The usefulness of these kinds of studies is that we can begin to characterize the short-term observed feedbacks of the climate system using satellite observations or reanalysis products with hopes to validate the projected future changes in climate. However, short-term feedbacks and/or climate sensitivity may not necessarily be indicative of long-term climate feedbacks and sensitivity. This study characterizes the short-term variability of TOA flux anomalies over an ensemble of 20-year periods from the 20^{th} century AOGCM simulations, for ease of comparison with the available reanalysis record of 20 years. For any relationships between the short-term and long-term variability in climate models, the modeled short-term variability can then be checked against the observed short-term variability.

This thesis characterizes and compares climate feedback-related behavior over several time scales between a number of AOGCMs and a reanalysis observational product. The radiative kernel technique is used to compute TOA radiative effects of anomalies in feedback variables, that is water vapor, temperature, and surface albedo, from the 20^{th} century AOGCM simulations. The variability is characterized and separated into three time scales: annual cycle, interannual variability, and decadal trends.

Quantified characteristics of variability are compared across models and an observational data product and any relationships between time scales are explored. The agreement of variability between models and observational datasets will contribute to better confidence in the climate models skill at simulating current climate variability and future projections of climate change if any link between short and long time scales is found.

We find that the annual cycle provides a better constraint than interannual or decadal variability on global and hemispheric long-term feedbacks. For water vapor and atmospheric temperature, this result is strong for both the northern and southern hemispheres. For surface albedo, the strongest relationship between the annual cycle and long-term feedback occurs in the southern hemisphere. However, using the annual cycle to estimate the long-term feedback still results in a large uncertainty. For atmospheric temperature and water vapor, the reanalysis observations of the annual cycle are within the range of models, but for surface albedo, we find that the reanalysis annual cycle is smaller in magnitude than all models.

Chapter 2

Background and Literature Review

2.1 Earth's Energy Balance

The rate of change of the global temperature of the Earth is governed by the difference between the rate of absorbed solar radiation (ASR) and the rate of outgoing longwave radiation (OLR),

$$C\frac{dT}{dt} = Q_0(1-\alpha) - F \tag{2.1}$$

where C is heat capacity ($JK^{-1}m^{-2}$) of the climate, and T is the global average surface air temperature. The first term on the right hand side of equation (2.1) is the absorbed solar radiation, Q, which is the fraction of the total incoming solar radiation, Q_0, that is not reflected by the Earth. The reflectivity, or albedo (α), of the Earth is about 0.3 on average. In the second term, F represents the total outgoing longwave radiation at the top of the atmosphere (TOA). Units of radiation are in Wm^{-2}. The difference between the absorbed solar radiation and the outgoing longwave radiation is the net radiative imbalance, R, at the top of the atmosphere, such that $R = Q - F$. In a steady state, the change in temperature is zero ($\frac{dT}{dt} = 0$, $R = 0$) such that the energy entering the system at the top of the atmosphere balances the energy exiting the system at the top of the atmosphere. That is, $Q = F$. This equilibrium state is described by the statistically steady global average surface temperature, T. If the Earth were not in equilibrium ($\frac{dT}{dt} \neq 0$), then $R \neq 0$ and $Q \neq F$.

The Earth's radiative energy balance is an important framework for understanding climate change on a global scale. Any net positive (negative) imbalance of the Earth's global energy flux at the top of the atmosphere, that is $R \neq 0$, averaged over a number of years leads to a warming (cooling) of the planet. In fact, over the period 2000-2004, measurements of global radiative energy flows reveal that the Earth is out of

balance, retaining $\approx 0.9\ Wm^{-2}$ in the Earth system (Trenberth et al., 2009). The Earth system retains energy by absorbing more (reflecting less) of the incoming solar radiation, or through a reduction in the OLR by increased infrared absorption by the atmosphere (e.g. increased concentrations of carbon dioxide). Higher atmospheric concentrations of CO_2 and other infrared absorbing gases force the climate to warm. The initial amount of energy kept in the system from, say, instantaneously doubling the concentration of CO_2 concentration is known as the radiative forcing, ΔG, of the climate. Changes in the TOA energy balance is given by (Bony et al., 2006):

$$\Delta R = \Delta G + \lambda \Delta T \tag{2.2}$$

The climate system's equilibrium response (when $\Delta R = 0$) to a sustained radiative forcing is proportional to the radiative forcing by (Roe, 2009):

$$\Delta T = -\lambda \Delta G = -\frac{1}{\gamma} \Delta G \tag{2.3}$$

The constant of proportionality, λ, is called the feedback parameter, which is the strength of the internal climate processes that affect the TOA energy balance, and is in units of $Wm^{-2}K^{-1}$. The inverse of the feedback parameter is called the climate sensitivity, γ, which is the increase in temperature due to a radiative forcing and has units of K/Wm^{-2}.

2.2 Climate Sensitivity & Feedbacks

A standard measure of climate sensitivity, known as the equilibrium climate sensitivity (ECS), is defined as the resulting equilibrium change in globally averaged surface air temperature (climate response) after doubling the amount of carbon dioxide in the atmosphere and letting the climate model run until a new equilibrium is reached. The radiative forcing due to an instantaneous doubling of CO_2 is estimated to be 3.7 Wm^{-2} (Kiehl, 2007). Because the ECS is calculated between changes in two equilibrium states, it is only defined for Atmospheric Global Climate Models (AGCMs) coupled to a slab-ocean models. A slab-ocean model is a simple ocean modeling component that communicates with the atmosphere model component through a mixed-layer temperature. A coupled Atmosphere-Ocean Global Climate Model (AOGCM) has a dynamic, multi-layer ocean model so it takes millennia in model years for an AOGCM to reach equilibrium. For this reason, simpler and related AGCMs are used

for calculating ECS because it takes less than 100 years to reach equilibrium. According to the 4th Assessment Report (AR4) of the IPCC, the current range in ECS among state-of-the-art AGCMs is 2.1 - 4.4 K with a likely value of 3.2 K (Randall et al., 2007). This range in ECS is due to varying feedback strengths across climate models.

The sum of the feedback strengths is the feedback parameter such that

$$\lambda = \lambda_T + \lambda_Q + \lambda_\alpha + \lambda_C + \epsilon \tag{2.4}$$

where λ_T is the total temperature feedback, λ_Q is the total water vapor feedback, λ_α is the surface albedo feedback, λ_C is the cloud feedback, and ϵ contains the cross-feedback terms and is assumed to be small, $\approx$10% (Shell et al., 2008). The total temperature feedback can be separated as: $\lambda_T = \lambda_{TS} + \lambda_{TA}$ where λ_{TS} is the surface temperature feedback and very similar from one model to the next (Soden and Held, 2006). The atmospheric temperature feedback can be separated as: $\lambda_{TA} = \lambda_0 + \lambda_L$, where λ_0 is the Planck feedback and is also essentially constant between models (Soden and Held, 2006). The spread in the temperature feedback among models comes from the lapse rate feedback, λ_L. The atmospheric temperature feedback is computed in this thesis, and is related to the lapse rate feedback by subtracting the Planck response, which is a uniform temperature increase throughout the entire atmospheric column, though the increase varies regionally, from the atmospheric temperature feedback. The lapse rate feedback is negative because the atmosphere warms more than the surface due to release of latent heat by condensation of moist air. The water vapor feedback has a SW and LW component. While the SW component is non-negligible, the LW component is dominant and is analyzed in this thesis.

As described earlier, the surface albedo and water vapor feedbacks are positive in that the initial climate response is amplified. All climate models produce positive albedo and water vapor feedbacks. The albedo feedback is the smallest feedback in the climate system with a mean and range of 0.26 $\pm$ 0.08 $Wm^{-2}K^{-1}$, and the water vapor feedback (1.8 $\pm$ 0.18 $Wm^{-2}K^{-1}$) is the largest. The only negative feedback is the lapse-rate feedback with a mean and range of -0.84 $\pm$ 0.26 $Wm^{-2}K^{-1}$. The cloud feedback is the most uncertain feedback among climate models with a mean and range of 0.69 $\pm$ 0.38 $Wm^{-2}K^{-1}$ (Bony et al., 2006). While the largest contribution to the uncertainty in climate sensitivity among models is from the cloud feedback, the spread in the water vapor and albedo feedbacks are substantial contributors (Bony et

al., 2006). If we assumed a climate sensitivity of 3 K, the TOA flux changes due to each of the feedbacks would be 5.4 Wm^{-2} for water vapor (i.e. $1.8Wm^{-2}K^{-1} \cdot 3K = 5.4Wm^{-2}$), 0.78 Wm^{-2} for surface albedo, 2.07 Wm^{-2} for clouds, and -2.52 Wm^{-2} for lapse rate. Compared to the initial radiative forcing of 3.7 Wm^{-2}, these feedbacks are important, especially the water vapor feedback. If we summed all the TOA flux changes together we'd get a total flux change due to feedbacks of 5.73 Wm^{-2} which is 1.5 times the original forcing.

The actual climate system is not in equilibrium so an effective climate sensitivity (EfCS) is used. The EfCS represents the global climate response if the transient state were run to equilibrium assuming constant feedback strengths (Randall et al., 2007). The EfCS is the strength of climate feedbacks at a particular time and may vary with forcing history and climate state (Randall et al., 2007). The climate sensitivity is assumed to be independent of base state although some studies (Jonko et al., 2011) show that the climate sensitivity indeed depends on the base climate state. However, in the present study, the 20^{th} century climate state is used, so differences in the base climate state between models are small and we can assume the climate sensitivity and thus feedbacks to be constant. When using observations to estimate the climate sensitivity, the effective climate sensitivity is being inferred. The EfCS can also be calculated from transient simulations of coupled atmosphere-ocean global climate models (AOGCMs) that have a fully dynamic, multi-layer ocean model component (Randall et al., 2007). Gregory et al. (2004) introduce a simple technique to calculate climate sensitivity from transient states in climate models and observations.

A common motivating question for all of the following studies, including the present, is to determine the climate sensitivity of the Earth. Because the sensitivity of the climate is unknown, GCMs are used to explore the possible range of climate sensitivity. Several studies (e.g. Colman, 2003a; Soden and Held, 2006; Soden et al., 2008) explore the uncertainty of individual climate feedbacks that contribute to the range in modeled climate sensitivity. Other studies estimate the climate sensitivity, feedback strengths, and TOA flux variability from satellite observations (e.g. Forster and Gregory, 2006; Gregory et al., 2004). Another way to approach the 'constraining climate sensitivity' problem is by exploring relationships between short-term and long term feedbacks and TOA radiative perturbations in models and observations (e.g. Hall and Qu, 2006; Knutti et al., 2006; Dessler, 2010). This thesis explores the variability of individual climate feedback radiative perturbations at the TOA by quantitatively characterizing variability of TOA fluxes due to three feedback variables:

- Atmospheric Temperature
- Water Vapor
- Surface Albedo

over three time scales:

- annual
- interannual
- decadal

Relationships between feedbacks in short and long time scales in AOGCMs are explored, and modeled variability on short time scales are compared with variability in equivalent record lengths of a reanalysis observational product. The following sections review the recent studies of feedbacks derived from climate models and observations and long-term climate feedbacks inferred from short-term feedbacks.

2.3 Observational Studies

Establishing an observed record of TOA radiative flux anomaly variability (SW, LW, & Net) as a benchmark for climate model performance is important because accurate simulations of the TOA flux variability on a global scale are needed for improving future climate change projections. Models can then be tested against these observations and should be able to accurately model the variability especially on a global scale (Harries and Belotti, 2010). Because there is substantial transport of heat away from the tropics, a global domain is needed to discern TOA flux variability in relationship to climate change studies. Trenberth et al. (2010) find relationships between tropical sea surface temperature and near global TOA flux anomalies and conclude that climate sensitivity discerned from only tropical radiation measurements could be misleading. If a climate feedback contributes to the overal climate sensitivity, it must be seen in global quantities (Slingo et al., 2000).

Wielicki et al. (2002) analyzed satellite observations of tropical longwave radiative fluxes from seven broadband instruments spanning 22 years from 1979 to 2001. Flux anomalies were calculated relative to the 1985-1989 base period. In the LW, large variations of up to 8 Wm^{-2} during the 1998 El Niño and a decadal change of 3.1 Wm^{-2} over the 1980s and 1990s were seen. This large decadal variability is significant

especially since radiative forcings of 1 Wm^{-2} are important for climate change scales. They concluded that the large decadal variability was due to variability in tropical cloudiness. After correcting some discovered biases in the ERBE data, Wong et al. (2006) find the LW decadal variability to be 1.6 Wm^{-2} over the same period. They also find interannual variability of near-global net TOA radiative flux anomalies in the 1990s was $\approx$ 1.5 Wm^{-2}. Harries and Belotti (2010) reanalyze the observed variability of the global net TOA radiative energy balance to determine its usefulness as a measure of climate change detection. Using broadband measurements of absolute fluxes measured by several satellites (ERBE & CERES), Harries and Belotti (2010) define a flux anomaly to avoid the poor absolute accuracy of flux values. They find that the interannual variability of $\pm$ 1.5 Wm^{-2} could result from errors other than absolute calibration. Scales and magnitudes of variability of Earth's TOA energy balance, as reported by Harries and Belotti (2010), include: volcanic eruptions that act over a few years to cause an imbalance on the order of -10 W/m2, interannual variations of 2 to 4 years with imbalances in the range of a few Wm^{-2} (although this is within the range of absolute errors of the instruments), and high frequency variability of 1-2 months in on the order of $\pm$ 4 Wm^{-2} (probably due to cloud variability). Global net TOA flux anomalies, excluding volcanic eruptions, usually fall within a few Wm^{-2} around zero. As a climate change measure, detecting a 1 Wm^{-2} TOA net flux change against natural variability with just the twenty years of satellite data is not yet reliable (Harries and Belotti, 2010). As Hansen et al. (2005) notes, on long time scales the Earth has likely been in balance within a fraction of 1 Wm^{-2} because a sustained imbalance of this magnitude over 10,000 years is enough to raise the ocean temperature by 100 K.

Forster and Gregory (2006) use the near global (60°N to 60°S) ERBE satellite flux data to extract effective climate sensitivity and the shortwave and longwave components using a linear regression analysis, following Gregory et al. (2004), of net TOA energy imbalance against surface air temperature. The slope of the regression line gives a value for the total feedback parameter. They find a climate feedback parameter of 2.3 $\pm$ 1.4 Wm^{-2} which corresponds to a climate sensitivity of 1.0-4.1 K. Forster and Gregory (2006) argue that feedback parameters derived from regressions of TOA flux anomalies and surface air temperature anomalies over short-term periods are likely representative of feedback parameters of long-term climate change, if the span of surface temperature change on the short-term is like that of long-term trends and temperature changes on the short-term behave like those expected for long-term

changes (i.e. temperature changes throughout the troposphere). Dessler et al. (2008) estimate the water vapor feedbacks over 2003-2008 using satellite observations of specific humidity from NASA's Atmospheric Infrared Sounder (AIRS) and find a positive mean feedback of 2.04 $Wm^{-2}K^{-1}$ (0.94 to 2.69) which is consistent with climate models. Flanner et al. (2011) derive an estimated range of the observed albedo feedback over the period from 1979 to 2008. They conclude that the northern hemisphere albedo feedback is between 0.3 and 1.1 $Wm^{-2}K^{-1}$ which is a larger range than climate model estimates.

2.4 Modeling Studies

Over a period of years, a net imbalance in the TOA global energy balance of a constant sign will lead to a change in climate, usually represented by a change in the globally averaged surface air temperature. Coupled atmosphere-ocean global climate models (AOGCMs) are used to project such future climate changes based on particular scenarios of greenhouse gas emissions that result in particular magnitudes of energy imbalances at the top of the atmosphere. The projected future warming of the climate depends on the future scenario used for input in the climate model and also the sensitivity of the modeled climate. AGCMs are also used to calculate ECS and feedbacks.

Colman (2003a) compared climate feedback results between several AGCMs by presenting a summary of published results of experiments where the concentration of CO_2 was instantaneously doubled and the AGCM was run until reaching a new equilibrium. Of the $2\times CO_2$ AGCM experiments included in Colman (2003a), the mean water vapor feedback was 1.7 $Wm^{-2}K^{-1}$ with a large range of 1.1 to 2.4 $Wm^{-2}K^{-1}$. The mean albedo feedback was 0.3 $Wm^{-2}K^{-1}$ with a large total range of 0.45 $Wm^{-2}K^{-1}$. While the cloud feedback contributes most to the spread of the total feedback, uncertainties in water vapor and albedo feedbacks are important as well (Colman, 2003a). Soden and Held (2006) calculated climate feedbacks in 14 coupled AOGCMs used for the IPCC AR4 with a doubling of CO_2 experiment (SRES A1B scenario). See Section 2.2 for values.

2.5 Motivation to compare short-term & long-term TOA flux anomalies

To constrain estimates of climate sensitivity, many studies have attempted to relate seasonal (e.g. Hall and Qu, 2006; Knutti et al., 2006) and interannual (e.g. Colman and Power, 2010) feedbacks to long-term feedbacks in climate. Feedbacks diagnosed from short time scales are then compared with observations. All these studies use GCMs to explore feedbacks over time scales because long time scales are only available with GCMs. The justification for exploring this relationship is that the seasonal sensitivity and climate sensitivity are governed by the similar processes. For example, snow accumulates over the winter and as temperatures warm into the spring, snow melts so the snow cover changes with seasonal temperature. In a warmer world, there may be less snow cover in general because precipitation may fall more often as rain rather than snow.

Colman (2003b) explored seasonal contributions to climate feedbacks in one AGCM. He found that the global LW water vapor feedback does not vary much seasonally and the LW lapse rate feedback contributes the most seasonal variation in feedbacks. The surface albedo feedback is more seasonally variable than the longwave feedbacks and the cloud feedback has the most seasonal variability. These results suggest that feedback seasonality is an important factor in the equilibrium climate sensitivity. Since water vapor shows little seasonal variation, the global water vapor feedback calculated at any point in the year might be a good estimate of the seasonal mean feedback (Colman, 2003b). Taylor et al. (2011) used a coupled AOGCM (CCSM3) to investigate climate feedback seasonality. They found little seasonality in the water vapor feedback, consistent with Colman (2003b), but the largest seasonal amplitude variation occurs in the Northern Hemisphere. The largest contribution to the long time, global average water vapor feedback occurs near the equator during April and May. The strongest seasonal variability of the lapse rate feedback occurs in the northern polar region, and a similar, and lesser behavior occurs in the southern polar region. The largest seasonal contribution to the long time global average lapse rate feedback occurs in the high latitudes during winters. The surface albedo feedback seasonality is most pronounced in the high latitude regions and the greatest contribution to the global average surface albedo feedback occurs during the summer in high latitudes. In fact, the largest contribution to the long time global average surface albedo feedback occurs in April in the mid-latitude northern hemisphere and is associated with snow

melt seasonality (Taylor et al., 2011). This is consistent with a study by Hall and Qu (2006).

Hall and Qu (2006) find a linear relationship in CMIP3 models between the spring-time snow albedo change (April to May difference) per temperature change of the Northern Hemisphere and the climate change albedo change per temperature change between the 20^{th} and 22^{nd} century April albedo. By comparing an ensemble of modeled snow albedo seasonal cycle feedbacks with observed values, they identify models that occur within this range and those with large biases. "Exploiting similarities between the seasonal cycle and anthropogenic climate change is a promising strategy for constraining other radiative feedbacks affecting the extratropics, where seasonality is most pronounced" (Hall and Qu, 2006). Similarly for surface temperature, Knutti et al. (2006) find a relationship between the amplitude of the seasonal cycle in Northern Hemisphere regions (where seasonal cycle is most pronounced) and the associated climate sensitivity.

However, according to Slingo et al. (2000), interannual time scales instead of seasonal time scales might be better suited to diagnose longer term feedbacks. The following studies calculate interannual time scale feedbacks from climate models and observations and show that they are reasonable estimates of century long feedbacks in models. Colman and Power (2010) examine radiative feedbacks in a coupled AOGCM from two experiments. The first experiment is a century-scale transient warming from a 1%/year CO_2 increase and the second is a natural, unforced simulation. The study seeks to understand how climate change feedbacks differ from those operating at interannual variability time scales. For the 'transient' simulations, they find that the transient feedbacks approximate feedbacks under equilibrium warming in AGCMs. The water vapor feedback derived from interannual 'unforced' variability is found to be about two-thirds of the 'transient' feedback. Interannual net lapse rate feedback is essentially zero while the 'transient' feedback strength is dominantly negative. The surface albedo feedback operating under interannual variability is found to be more strongly positive than the 'transient' feedback, and that is probably due to strong negative feedbacks due to Antarctic sea ice changes (Colman and Power, 2010). Chung et al. (2010) analyze relationships between surface temperature and TOA radiative fluxes, called radiative damping rates, in climate models and observations over the period 1985-1999. They find good agreement between between models and observations. They also show that the damping rates calculated from interannual variability

are "modestly correlated to the climate sensitivity of the model in response to increasing CO_2." The idea that motivates these studies is that the physical processes that contribute to the inter-model spread of climate sensitivity and feedbacks may be accounted for in the interannual variability of feedbacks or feedback related TOA effects, especially for water vapor and surface albedo, and may provide some information about long-term climate change feedback strength.

On the other hand, a few studies suggest that short time scale estimates of climate feedbacks may not be representative of long-term climate change feedbacks. Using short-term data to calculate the total feedback parameter and/or climate sensitivity may not be reliable if the fast feedback components do not represent the total climate feedback parameter (Lin et al., 2011). Forster and Gregory (2006) suggest that if their total feedback parameter is calculated from tropical variability and ENSO, it may not be representative of climate change feedback parameter. In fact, Dessler and Wong (2009) find that the water vapor feedback inferred from ENSO-driven variability in climate models and reanalysis observational products are larger than the water vapor feedback for long-term climate changes. Dessler (2010) finds no relationship between short-term and long-term cloud feedbacks within models though he finds similar short-term feedback values calculated in models and observations.

2.6 Objectives

This thesis further explores this issue of using TOA radiative perturbations due to feedback variables derived from annual and interannual time scales as 'proxies' for long-term climate change feedbacks. This study breaks down the TOA radiative flux anomalies into components due to radiatively active climate variables such as temperature, water vapor, and surface albedo. By, first, quantifying characteristics of the annual, interannual and decadal variability of model TOA flux anomalies over the 20^{th} century and comparing the characteristics over a short and long time period, this thesis contributes to the discussion of the following questions:

- Does the short-term variability in feedbacks and TOA flux anomalies tell us anything about long-term feedbacks and trends in TOA flux anomalies?
- Can climate sensitivity components be constrained by this analysis method?

Chapter 3

Data

3.1 Climate Models

Climate models simulate the general circulation of the atmosphere and ocean by numerically solving the Navier-Stokes equations of motion on a rotating, spherical grid. There are climate models of varying complexity used for different purposes. Simple models, with fewer components and processes included, are used to isolate and understand the evolution of a single process or phenomenon of the ocean and atmosphere. The most complex models, with fully-coupled components (e.g. ocean, atmosphere, land, and sea ice), are used to simulate the current climate and make projections of the future evolution of the climate system. These models (e.g. AGCMs and AOGCMs) are used to study climate sensitivity and feedbacks. The basic components of an AOGCM include atmosphere, ocean, sea ice, and land models. The atmospheric model includes a radiation scheme to account for the movement and exchange of radiative energy from the top of the model to the surface. Computational infrastructure and numerical methods limit the grid resolution used in climate models. Generally, global climate models have a horizontal resolution on the order of 1°-4° latitude and longitude and are able to resolve large scale dynamics on the order of greater than 100 km. Processes that occur on scales smaller than the grid resolution that affect the large scale dynamics are not explicitly resolved but parameterized based on physical and empirical constraints. Examples of parameterized processes include clouds, ocean eddies, and sea ice melt ponds.

Table 3.1: Coupled Atmosphere-Ocean Global Climate Models used in this study. First column contains the model abbreviation, second column contains modeling institution, third column contains the number of ensemble members.

Abbreviation	Climate Modeling Institution	Runs
CCSM	NCAR Community Climate System Model 3.0	8
CGCMT47	Canadian Centre for Climate Modeling & Analysis v. 3.1	5
CGCMT63	Canadian Centre for Climate Modeling & Analysis v. 3.1	1
CM20	Geophysical Fluid Dynamics Lab Climate Model 2.0	3
CM21	Geophysical Fluid Dynamics Lab Climate Model 2.1	3
ECHAM	Max Planck Institute for Meteorology v. 5	3
GISSAOM	NASA Goddard Institute for Space Science – AOM	1
GISSEH	NASA Goddard Institute for Space Science – EH	5
GISSER	NASA Goddard Institute for Space Sciences – ER	9
INM	Institute for Numerical Methods Model 3.0	1
IPSL	Institut Pierre Simon Laplace Climate Model 4	1
MIROCHI	Center for Climate System Research (Japan) v. 3.2 hi-res	1
MIROCMED	Center for Climate System Research (Japan) v. 3.2 med-res	3

3.2 20^{th} century simulations (20C3M)

The climate model data used in this study were generated by fully-coupled Atmosphere-Ocean Global Climate Models for the Third Climate Model Intercomparison Project (CMIP3) used in the findings presented in the Fourth Assessment Report (AR4) of the Intergovernmental Panel on Climate Change (IPCC). We use the data from 13 of the climate models that simulated the 20^{th} century climate (20C3M). Each climate model has a unique combination of horizontal and vertical resolutions, complexity of climate system components, radiative transfer scheme, and sub-grid scale parameterizations. Table 3.1 lists the modeling institutions, climate model abbreviation and number of ensemble members used.

The 20^{th} century climate simulation is used as the initial conditions for simulations of future climates. The ability of climate models to represent the 20^{th} century climate with some degree of accuracy gives some confidence that processes will be accurately

represented in future climate projections (Randall et al., 2007). The 20C3M simulation was initialized from a control model simulation and forced by observed land changes and estimated natural and anthropogenic radiative forcings during the 20^{th} century including solar irradiance cycle, historic volcanic eruptions, and increases in carbon dioxide to name a few. However, the radiative forcing components included is not the same for all climate models. See model documentation including radiative forcing information for the climate models of the CMIP3 archive here: http://www-pcmdi. llnl.gov/ipcc/model_documentation/ipcc_model_documentation.php. Listed in Table 3.2 are the atmosphere and ocean spatial resolutions and the equilibrium climate sensitivity of the corresponding slab-ocean Atmospheric GCM.

The variables used are surface albedo, atmospheric temperature, and specific humidity. The surface albedo is the fraction of the incident sunlight reflected by the surface. Sea ice and land snow evolve throughout a simulation given the dependence on temperature and other atmosphere and ocean properties. The albedo of the surface evolves with time based on surface cover changes. Atmospheric temperature is in units of Kelvin. The specific humidity is in units of kg (water vapor)/kg (air).

3.3 ECMWF ERA-Interim

The observational dataset used in this study is the ERA-Interim reanalysis product provided by the European Center for Medium Range Weather Forecasts (ECMWF). This reanalysis dataset is derived by assimilating observational data into a forecast model to produce the global state of the atmosphere from 1979 to the present. Satellite and in situ observations are used as input to the data assimilation. Various satellite instruments provide measurements of radiances and atmospheric motion vectors. Air temperature, wind, and specific humidity measurements are provided by radiosonds, aircraft, and wind profilers. Surface pressure and 2-meter temperature data are available from ships, buoys, and land stations. The data assimilation method used for ERA-Interim is a 12-hourly four-dimensional variational analysis (4D-Var). Data is assimilated during successive 12-hour cycles. Prior information from a forecast model for the physical evolution of atmospheric variables is combined with available observations at each 12-hour cycle to produce an estimate of the physically constrained evolution of the state of the atmosphere and surface. The forecast model is important because it can extrapolate in a physically meaningful way to regions where direct

Table 3.2: AOGCM specifications. Second column contains the top most atmospheric level resolved in the atmospheric component, followed by the number of atmospheric levels in parenthesis, and the horizontal resolution in degrees of latitude by longitude followed by the triangular spectral truncation in parenthesis. The third column contains the horizontal resolution in degrees of latitude by longitude of the ocean component and vertical levels in parenthesis. The fourth column contains the equilibrium climate sensitivity (ECS), using the corresponding slab-ocean model, and the transient climate response (TCR). This information can be found in Tables 8.1 and 8.2 of the IPCC AR4 (Randall et al., 2007).

Model	Atmosphere Component	Ocean Component	ECS & TCR
CCSM	2.2 hPa (26) $1.4° \times 1.4°$ (T85)	$0.3° - 1° \times 1°$ (40)	ECS 2.7 K TCR 1.5 K
CGCMT47	1 hPa (31) $2.8° \times 2.8°$ (T47)	$1.9° \times 1.9°$ (29)	ECS 3.4 K TCR 1.9 K
CGCMT63	1 hPa (31) $\sim 1.9° \times 1.9°$	$0.9° \times 1.4°$ (29)	ECS 3.4 K TCR n/a
CM20	3 hPa (24) $2.0°\times 2.5°$	$0.3°$-$1°\times 1°$	ECS 2.9 K TCR 1.6 K
CM21	3 hPa (24) $2.0° \times 2.5°$	$0.3 - 1° \times 1°$	ECS 3.4 K TCR 1.5 K
ECHAM	10 hPa (31) $\sim 1.9° \times 1.9°$ (T63)	$1.5° \times 1.5°$ (40)	ECS 3.4 K TCR 2.2 K
GISSAOM	10 hPa (12) $3° \times 4°$	$3° \times 4°$ (16)	ECS n/a TCR n/a
GISSEH	0.1 hPa (20) $4° \times 5°$	$2° \times 2°$ (16)	ECS 2.7 K TCR 1.6 K
GISSER	0.1 hPa (20) $4° \times 5°$	$4° \times 5°$ (13)	ECS 2.7 K TCR 1.5 K
INM	10 hPa (21) $4° \times 5°$	$2° \times 2.5°$ (33)	ECS 2.1 K TCR 1.6 K
IPSL	4 hPa (19) $2.5° \times 3.75°$	$2° \times 2°$ (31)	ECS 4.4 K TCR 2.1 K
MIROCHI	40 km (56) $\sim 1.1°\times 1.1°$ (T106)	$0.2° \times 0.3°$ (47)	ECS 4.3 K TCR 2.6 K
MIROCMED	30 km (20) $\sim 2.8° \times 2.8°$ (T42)	$0.5° - 1.4° \times 1.4°$ (43)	ECS 4.0 K TCR 2.1 K

observations are lacking. The forecast model used for the ERA-Interim reanalysis product is the ECMWF Integrated Forecast System, which consists of fully coupled atmosphere, land surface, and ocean wave components (Dee et al., 2011). The global atmospheric fields used in this study are monthly averages of the atmospheric temperature and specific humidity from 1000mb to 10mb. The surface variables used are monthly averages of forecast albedo and 2-meter above surface air temperature. The years used for this thesis are the 20 years spanning 1989-2008.

3.4 Data Preprocessing

Since each dataset, from climate models and the reanalysis, has a different horizontal and vertical resolution, we begin by regridding the data onto a common grid of 17 vertical levels (10, 20, 30, 50, 70, 100, 150, 200, 250, 300, 400, 500, 600, 700, 850, 925, 1000mb) and a horizontal resolution of T42 (approximately 2.8° latitude by 2.8° longitude), the same grid as the CAM radiative kernels.

Since we are interested in specific humidity concentrations as they affect the radiative energy balance, we use the natural log of specific humidity as the variable because water vapor absorption of longwave radiation behaves like the natural log of specific humidity. After regridding the variables to a common grid of T42 horizontal resolution, we use surface albedo (α), atmospheric temperature (ta), and water vapor ($\ln(q)$) as our feedback variables. Water vapor and atmospheric temperature have values on all 17 vertical levels. All variables are monthly averages from each year of the simulation. The 100-year period from 1901-2000 (sometimes 1900-1999 if year 2000 was not present in the model's file output) is the data used in this analysis. This 100-year period is analyzed in two ways. First, for each run of each model used in this analysis, the TOA flux anomalies and statistical characteristics of variability are computed for the entire 100-year period. Second, the 100-year period is separated into five sequential, non-overlapping 20-year slices. For example, if climate model X is run three times, then fifteen 20-year slices will result for model X. The same analysis is then performed on each 20-year slice for each run for each model.

Chapter 4

Methods

The goal of this work is to quantify the variability of TOA flux anomalies due to atmospheric temperature, water vapor and surface albedo over several time scales. To convert the anomalies in feedback variables to the net TOA effect, we need a method to calculate feedbacks. We first discuss several feedback calculation methods (Section 4.1), then expand in more detail the method used in this thesis (Section 4.2). We describe how TOA flux anomalies are computed (Section 4.3) and how variability is quantified on annual, interannual, and decadal time scales (Section 4.4). The final section (4.5) describes the regression method used to compare characteristics of feedback variability.

4.1 Methods of Calculating Climate Feedbacks

There are several ways to calculate radiative feedbacks. The first is the partial radiative perturbation (PRP) technique (Wetherald and Manabe, 1988). Given two climate states, a control climate and a doubled CO_2 climate, the perturbed variable field from the doubled CO_2 climate is inserted in place of the control field. The PRP method then uses an offline radiation code to calculate instant TOA radiative flux changes for perturbations of one variable at a time leaving all other variables unchanged. This method assumes variables are temporally uncorrelated. Large biases in calculated feedbacks could result for variables that are indeed correlated, like water vapor and clouds (Soden et al., 2008). The advantage of the PRP method is that it accounts for some of the non-linear relationships among variables. A disadvantage is that specific humidity, temperature, cloud and surface albedo fields become decorrelated introducing errors in the feedback estimate. The PRP technique is also computationally expensive having to run a radiation code every time. The second is

the Gregory method from Gregory et al. (2004) where TOA flux anomalies (generally LW, SW, and net) are regressed against global average surface air temperature anomalies. The slope of the linear regression is the feedback strength in $Wm^{-2}K^{-1}$. The advantage of the Gregory method is its simplicity and the fact that it can be used for both model and observational data. A disadvantage is that it only separates the net feedback strength into SW and LW components. The radiative kernel technique (RKT) is described in the following section. Its advantages are that it can be used for model and processed observational fields, it is quick and easy to implement in multiple situations once the radiative kernel is calculated, and it can be used to calculate not only SW and LW components of the feedback strength, but also components due to water vapor, surface albedo, temperature, and clouds. We use the radiative kernel technique and perform selected calculations using the Gregory method.

4.2 Radiative Kernel Technique

Soden et al. (2008) introduced a new technique for feedback calculation, called the radiative kernel technique, that decomposes the feedback into the TOA response to a standard change in a feedback variable (the 'kernel') and climate response. The radiative kernel technique is an efficient way to calculate feedbacks and eliminates the issue of cross-field correlations. The radiative kernel technique calculates the TOA radiative effect of a perturbation to a single climate variable, namely x, which in this thesis is either water vapor, atmospheric temperature or surface albedo. The TOA radiative effect of changes in variable x, ΔR_x, is a function of x, which is a function of global average surface air temperature, T. So, $\Delta R_x = \Delta R_x(T)$. To approximate this function, $\Delta R_x(T)$ is expanded in a Taylor series about the base climate state, T_0.

$$\Delta R_x(T) = \Delta R_x(T_0) + \frac{d\Delta R_x(T_0)}{dT} \cdot (T - T_0) + \frac{d^2\Delta R_x(T_0)}{dT^2} \cdot \frac{(T - T_0)^2}{2} + \dots \quad (4.1)$$

The first term is zero, $\Delta R_x(T_0) = 0$, because at the base state, there is no relative change in variable x, and so no radiation change. The second term is of first-order and is the largest. The remaining higher-order terms, which account for non-linear behavior of feedbacks and are assumed to be small ($\approx 10\%$) and thus neglected in the kernel technique analysis. In other words, the radiative flux changes in the system

are assumed to be adequately described by this linear model. Thus, equation 4.1 becomes:

$$\Delta R_x(T) = \frac{d\Delta R_x(T_0)}{dT} \cdot (T - T_0) = \frac{\partial R_x}{\partial x}\left(\frac{dx}{dT}\right)\Delta T \tag{4.2}$$

The feedback strength for variable x is given by:

$$\lambda_x = \frac{\Delta R_x}{\Delta T} = \frac{\partial R_x}{\partial x} \cdot \frac{dx}{dT} \tag{4.3}$$

in terms of $Wm^{-2}K^{-1}$. The sum of all the feedback strengths is the feedback parameter from equation 2.4:

$$\lambda = \sum_x \lambda_x = \lambda_T + \lambda_Q + \lambda_\alpha + \lambda_C + \epsilon \tag{4.4}$$

where ϵ encompasses the cross-feedback terms, that is the interaction between feedbacks, and is also assumed to be small. In other words, the radiative kernel technique assumes that individual feedbacks combine linearly.

The first component on the right hand side of equation 4.3, $\frac{\partial R_x}{\partial x}$, is the radiative effect of a standard change in climate variable x. This component, called the radiative kernel, is calculated using an offline radiative transfer model. Figure 4.1 shows a schematic of the calculation of the radiative kernel. The Community Atmospheric Model Version 3 with specified climatological sea surface temperature and sea ice is run for a year, establishing the base climate state. Then, for each model level the base climate state is perturbed uniformly over the globe by a standard anomaly, x', while keeping all other variables constant. For the temperature kernels, the standard anomaly is one Kelvin. For surface albedo, it is a 0.01 increase of the surface reflectivity. For water vapor, the standard anomaly is the change in specific humidity due to a 1 K increase in temperature keeping relative humidity constant. This base climate with a single layer perturbation is input into the radiative transfer model of CAM3, and the output is the resulting change in the top of the atmosphere energy balance for each month and location.

Technically, the radiative kernel is the TOA flux change due to a standard change. Division by the standard anomaly, x' normalizes the flux anomaly and is appropriate. One benefit of using the radiative kernel technique, instead of the PRP method, to calculate feedbacks is that once the radiative kernels have been calculated, they can be used for myriad climate feedback studies across various models and observational

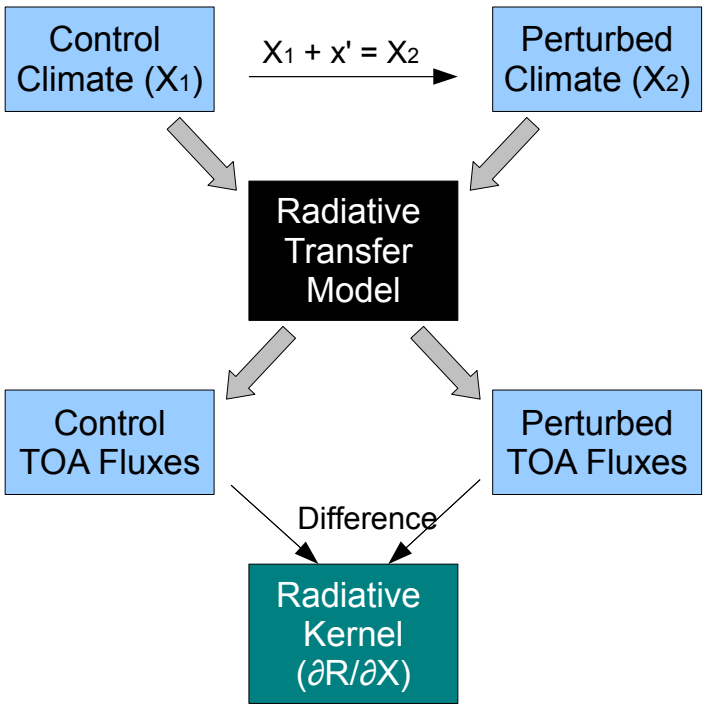

Figure 4.1: Schematic of radiative kernel calculation.

climate products of a similar base state. The second component of equation 4.3, $\frac{dx}{dT}$, is the climate system response to a change in temperature and is discussed in Section 4.3. The discrete form of the feedback strength is given by:

$$\lambda_x = K_x \left(\frac{\Delta x}{\Delta T} \right). \tag{4.5}$$

The radiative kernel ($K_x = \frac{\partial R_x}{\partial x}$) is already calculated (Shell et al., 2008), so only the change in the climate variable, Δx, given a change in climate, ΔT, is needed to calculate the feedback strength. Figure 4.2 shows the LW water vapor, atmospheric temperature, and surface albedo kernels, before division by the standard anomaly. The result of these calculations is a value at each latitude, longitude, level and month for the given variable's contribution to the TOA energy flows. Negative values in the top two rows indicate less energy trapped and thus a cooling TOA effect. Negative values in the surface albedo kernel are generally multiplied by negative albedo changes resulting in a positive warming effect. A warming TOA effect (positive Wm^{-2} value) can occur through a reduction of OLR (e.g. more atmospheric water vapor to trap more LW radiation) or an increase in ASR (i.e. less sea ice reflects less sunlight).

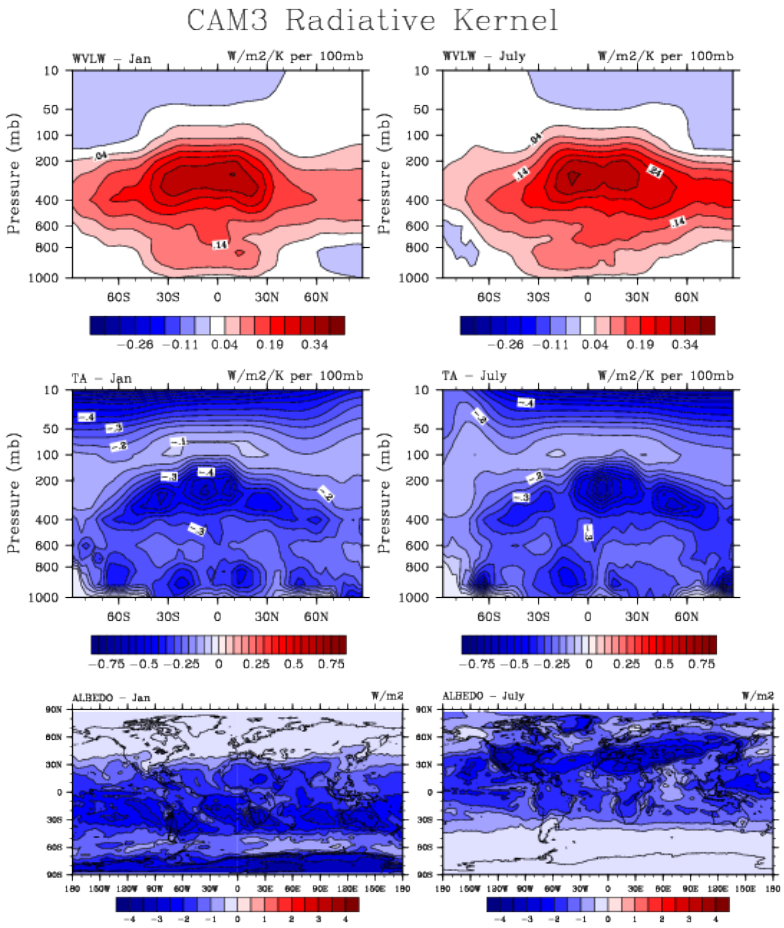

Figure 4.2: Zonal average radiative kernel for LW water vapor (top) and atmospheric temperature (center) for January (left) and July (right). Bottom plots are January and July surface albedo kernel and are in units of Wm^{-2} per fractional albedo change. Note different scales.

Conversely, a cooling TOA effect (negative Wm^{-2} value) can occur through an increase in OLR (e.g. reduction in water vapor or increase in atmospheric temperature) or a reduction of ASR (i.e. more sea ice reflects more sunlight).

The contributions to TOA energy flows, in Wm^{-2}, are summed from the surface to the top pressure level. Each level's contribution is weighted by the thickness of the layer, since the radiative kernel is calculated per 100mb. For the surface variables, the net TOA effect is the effect of the surface layer. The sign convention is such that positive values indicate more energy trapped in the system and thus a warming TOA effect.

Typically, feedbacks in climate models are calculated using the difference in mean climate states (averaged over at least 10 years) between a control climate that is in equilibrium and an experiment climate of a new equilibrium state after instantaneously doubling the concentration of carbon dioxide in the atmosphere, or the difference in mean climate state between two time periods not necessarily in equilibrium. The present study calculates feedbacks with reference to a climatology of a given period of time; essentially we examine the short time scale variability of feedbacks calculated using anomalies of climate variables around the mean state. The anomaly in the climate variable is: $\Delta x = x - x_{avg}$ and the anomaly in climate, as represented by temperature, is: $\Delta T = T - T_{avg}$, where x_{avg} and T_{avg} are the average seasonal cycle. This study looks at the short time scale variability not just in feedbacks, but in the corresponding top of the atmosphere radiative flux anomalies. These radiative anomalies are simply feedbacks calculated in the aforementioned way excluding the normalization by the anomaly in global surface air temperature (TAS). In equation form, the radiative anomaly at the TOA is defined as:

$$\Delta R_x = \lambda_x \cdot \Delta T = K_x \cdot \Delta x \tag{4.6}$$

With this framework, Δx can be calculated from model fields, reanalysis fields, or satellite fields so that the characteristics of the variability of the top of the atmosphere radiative anomalies due to each climate variable can be compared across models and observations of the climate system. We can't directly compare albedo changes to water vapor changes, but we can compare net TOA effects across variable fields.

4.3 TOA Radiative Flux Anomalies

This thesis compares the variability of top of the atmosphere flux anomalies due to three variables (water vapor, atmospheric temperature, and surface albedo) over two time lengths (20 years and 100 years) in the 20^{th} century climate model simulations. Variability of TOA flux anomalies are characterized instead of anomalies in the variables themselves because we are interested in the culminating TOA effect of anomalies throughout the atmosphere and surface. An advantage of this is that we are preserving the variability of anomalies at each grid point and converting it into a TOA effect that is additive (we are assuming that the TOA effects are indeed additive). It is a way of accounting for anomalies everywhere in their overall and cumulative effect on

the TOA energy balance. Also, we are ultimately interested in comparing short-term and long-term feedback variability so the variability in the TOA energy balance is conducive and convenient for that end.

The climate variable anomalies are calculated by first computing and removing the average seasonal cycle over the period of interest. The seasonal cycle was calculated by averaging all the Januarys, Februarys, etc, and then subtracted from each year of the 20-year or 100-year time series. For the 100-year period the average seasonal cycle from the entire record was removed from each year. For the 20-year slices, the average seasonal cycle of each 20-year period was calculated and removed from each year of the respective periods. The average seasonal cycle (January to December) is computed for each grid point and level of the model or reanalysis product. In the case of water vapor, we take the natural log of specific humidity, ln(q), to be the variable of interest because absorption of radiation by water vapor behaves like the natural log of water vapor. The average seasonal cycle of ln(q) is then subtracted from the field of ln(q). Figure 4.4 shows examples of the average seasonal cycle and is discussed further in Section 4.4.

The top of the atmosphere radiative flux anomalies are then calculated for each variable by multiplying the de-seasonalized climate anomaly by the corresponding radiative kernel, then dividing by the standard anomaly of the climate variable as described previously. The time series of TOA flux anomalies for each variable are then zonally and globally averaged for further analysis. Figure 4.3 demonstrates the progression by which TOA flux anomalies are calculated for water vapor for CCSM. First, plot (a) shows a 20-year time series of globally averaged specific humidity at 850 hPa in units of kg (water vapor) per kg (air). Next, we take the natural log of plot (a) which is shown in plot (b). Working with the natural log of specific humidity as the variable, we compute and remove the average seasonal cycle over the 20-year period to obtain anomalies shown in plot (c). Note that the scale of anomalies is much smaller than absolute values of water vapor before deseasonalizing. The radiative kernel technique is then used to compute the TOA effect of water vapor anomalies as shown in plot (d). Each of these steps were performed over a 3-dimensional domain. The area-averages are computed after obtaining a 3-dimensional field of TOA effects. Global averages at each step of the way are presented here for clarity. Area averaged TOA effects are then detrended before further analysis.

To obtain a time series of feedbacks from this time series of TOA radiative flux anomalies, one simply divides the TOA flux anomalies by the corresponding surface

air temperature anomalies. Statistical techniques are used to characterize the variability of the TOA radiative flux anomalies. Those characteristics, or metrics, are then compared across climate models and with an observationally-based reanalysis product.

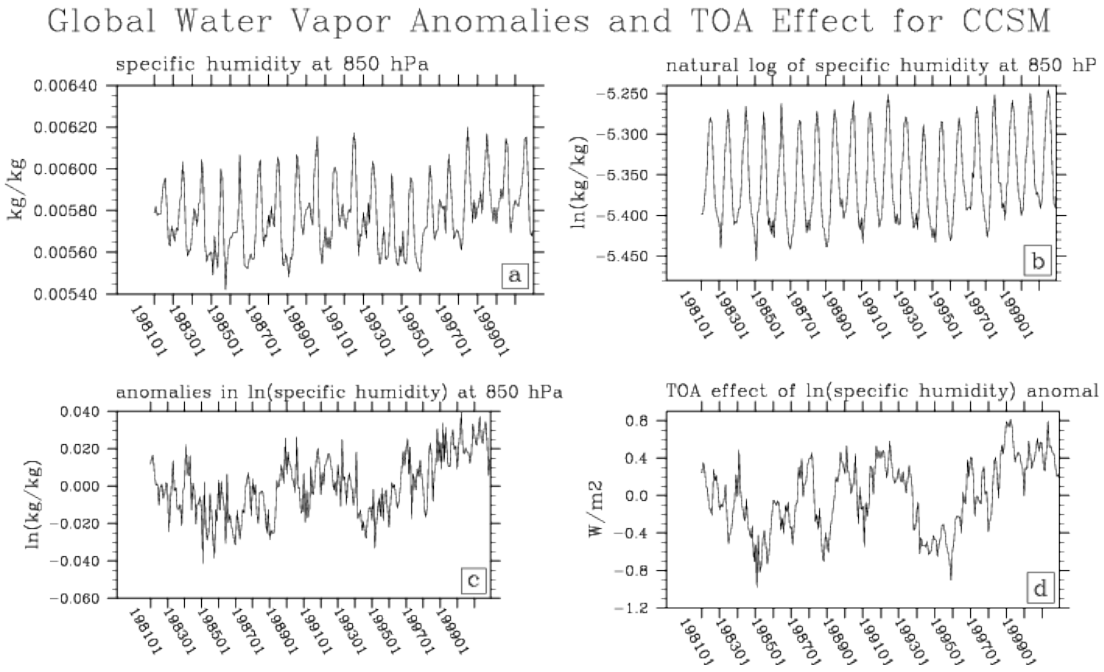

Figure 4.3: Anomalies and TOA Flux Anomalies for Water Vapor. Global average specific humidity values at 850 hPa are shown in plot a. Plot b shows the natural log of plot a. Plot c is the deseasonalized data from plot b. Plot d is the cumulative TOA effect of water vapor anomalies from all levels.

4.4 Quantifying Characteristics of Feedback Variability

Feedback variability is separated into and characterized by three time scales of interest: annual (within a year), interannual (1-10 years), and decadal (20-year and 100-year trends); and three geographic regions: global, northern hemisphere, and southern hemisphere. Statistical metrics are presented as an average and range of values of all runs (and slices, for the case of the 20-year periods) for a particular model. The general motivating question for studying variability of TOA flux anomalies at these three time scales is how short-term climate feedback variability is related

to long-term trends and feedbacks, with the ultimate goal of better projecting possible future climate.

Each 20-year slice can be thought of as a realization of the "observed" variability in TOA effects. Results for the 20-year slices are presented as an average and range of all slices for a given model. Analyzing the 20^{th} century simulations in this way is conducive to quantifying how much the variability at a 20-year time scale tells us about the variability on a century scale. How much can the current short observational record tell us about potential future variability and trends of the climate? In other words, are the trends in the observed 20 year periods due to natural variability or are they indicative of global warming? Of particular interest are any relationships in measurements of variability found between short-term (20-year) and long-term (100-year) periods because a goal of this thesis is to test how well any information about variability in the TOA flux anomalies (due to individual variables) obtained from a short record, analogous to the length of the observed record, is related to variability in TOA flux anomalies obtained from a long record.

Annual

The seasonal cycle was removed from the climate variable fields in the calculation of the climate anomaly for both the 20-year and 100-year periods (e.g. Figure 4.3). The seasonal cycle is averaged over the globe and the northern and southern hemispheres, weighted by latitude. For the three-dimensional variables (atmospheric temperature and specific humidity), the seasonal cycle at 850 hPa is used because it is a typical height of the boundary layer of the atmosphere. The northern hemisphere tends to dominate the seasonal cycles on the global scale because there is more land area in the NH and land responds quicker to temperature changes than the ocean.

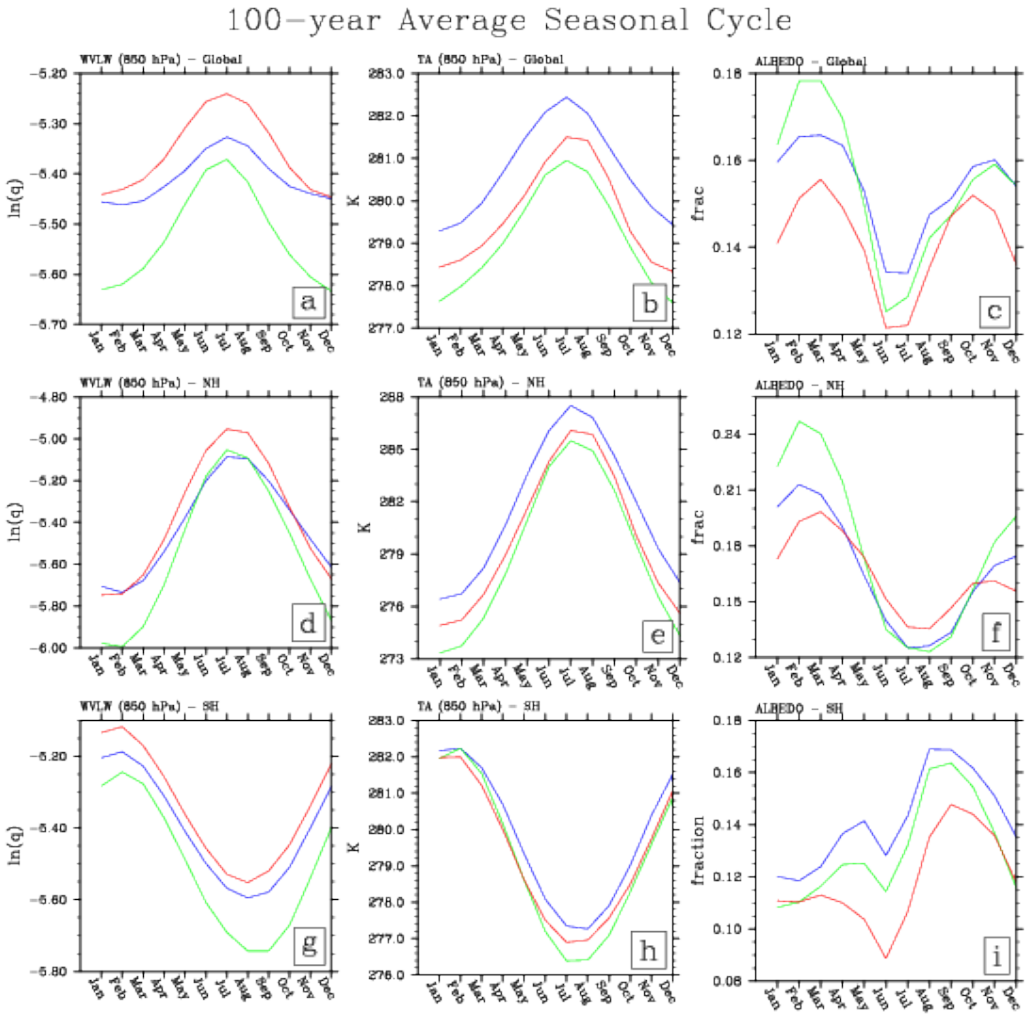

Figure 4.4: Average seasonal cycle over 100-year period of natural log of specific humidity at 850 hPa (left), atmospheric temperature at 850 hPa (middle), and surface albedo (right) for CCSM (blue), CM20 (green), and GISSER(red) for the globe (top), NH (middle), and SH (bottom).

The metric of variability for the annual time scale is the amplitude of the seasonal cycle. The amplitude of the seasonal cycle is defined differently for each variable and geographic area with the goal of capturing the maximum seasonal change. Seasonal amplitude definitions are summarized in Table 4.1. For water vapor, the global seasonal amplitude is defined as for temperature, the June-July-August average minus the December-January-February average. The northern and southern

Table 4.1: Summary of seasonal cycle amplitude definitions

Region	Water Vapor LW	Atm. Temperature	Surface Albedo
Global	JJA-DJF	JJA-DJF	FM-JA
N. Hem.	JAS-JFM	JJA-DJF	June-April
S. Hem.	JFM-JAS	JJA-DJF	August - June

hemisphere seasonal amplitudes are defined as the July-August-September average minus the January-February-March average and the January-February-March average minus the July-August-September average. See plots a, d, & g in Figure 4.4. For atmospheric temperature, the seasonal amplitude is defined as the difference between the summer and winter seasons, the June-July-August average minus the December-January-February average. (This definition follows from Knutti et al. (2006) linking northern hemisphere seasonal amplitude in temperature to climate sensitivity). See plots b, e, & h in Figure 4.4. For surface albedo, the global seasonal amplitude is defined as the average of the two maximum months (February and March) minus the average of the two minimum months (July and August) (plot c in Figure 4.4). The northern hemisphere seasonal cycle is defined as the change in surface albedo between April and June because it is the largest (negative) rate of change in the northern hemisphere surface albedo seasonal cycle (plot f in Figure 4.4). This is a similar definition to that used in the study by Hall and Qu (2006) where the northern hemisphere snow albedo percent change from April to May is used. The southern hemisphere surface albedo seasonal cycle is defined as the change from June to August, the largest (positive) rate of change (plot i in Figure 4.4). Note the differences in the magnitude of seasonal amplitude and mean values among the three models shown in Figure 4.4. When removing the seasonal cycle from feedback variable anomalies, the mean value is also removed so we are able to compare anomalies centered around a zero mean state for all models.

We also compute the corresponding seasonal amplitude of surface air temperature (TAS). We use this value to normalize the seasonal amplitude of the feedback variable. Since the feedback variables are dependent on surface air temperature changes (e.g. more ice melts for warmer temperatures), it is appropriate to normalize by the surface air temperature, especially for surface albedo. Normalizing the atmospheric temperature seasonal amplitude is not as meaningful because the temperature change

at 850 hPa should be very close to that at the surface. We don't expect normalizing the water vapor seasonal amplitude to be very meaningful since we are looking at the natural log of water vapor. However, normalizing by TAS seasonal amplitude and then comparing these normalized seasonal amplitudes with other normalized metrics adds in another factor that could explain any relationship. For example, if the surface air temperature seasonal amplitude is related to the TAS 100-year trend, then any relationship seen in the normalized water vapor amplitude and normalized water vapor 100-year trend, could be due to the relationship in the surface air temperature metrics and not the water vapor metrics themselves. For this reason, comparisons of non-normalized metrics are also presented when there is a large difference between comparing normalized and non-normalized metrics.

Interannual

On the interannual scale, we look at the standard deviation of TOA flux anomalies for each time series as a measure of the spread of the anomaly distribution. See Figure 4.6 (left plot). Before any statistical calculations are performed on the time series of area-averaged TOA radiative flux anomalies, the series is detrended. What remains are month-to-month fluctuations around the zero mean of the flux anomalies. For the 20-year time slices, a least square linear trend is calculated (plot a in Figure 4.5) and removed. The standard deviation is then computed from the resulting time series (plot c in Figure 4.5). For the 100-year time periods, a better fitting least squares quadratic trend is removed from the time series. The linear trend is also shown in plot b of Figure 4.5. The standard deviation is then computed for the quadratically detrended TOA flux anomalies (plot d in Figure 4.5). The standard deviation is calculated as:

$$\sigma = \sqrt{\frac{\sum_{i=1,n} \left(X_i - \overline{X}\right)^2}{n-1}}, \tag{4.7}$$

The standard deviation is calculated for each variable and each geographical area (global, NH, and SH) average and is in units of Wm^{-2}.

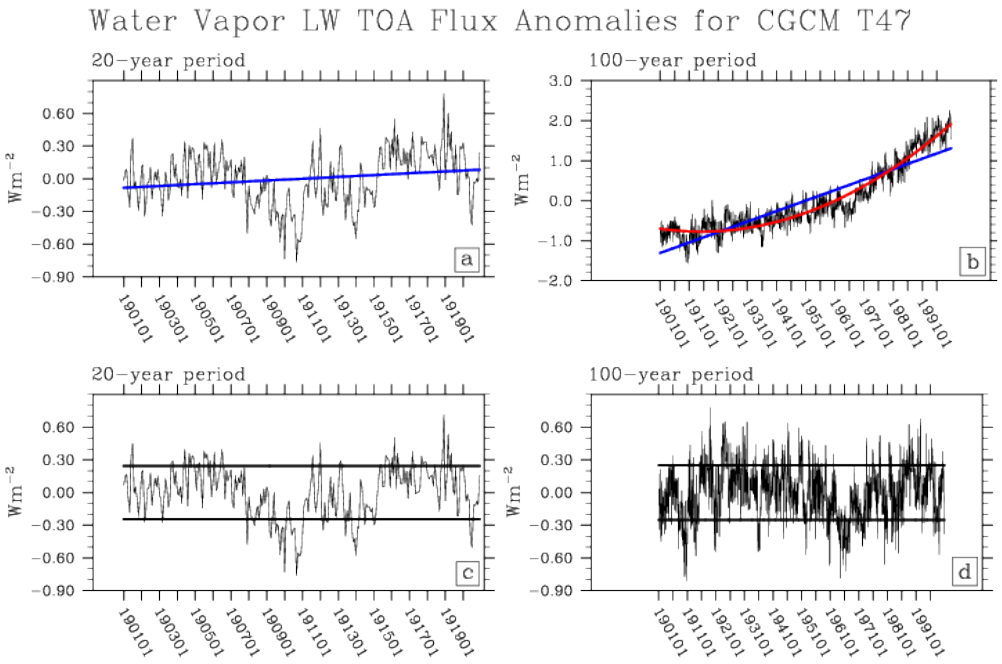

Figure 4.5: An example of a 20-year (left) and 100-year (right) global average time series of longwave water vapor TOA flux anomalies. The least square linear trend is shown in blue in plots a & c, but only removed from the time series in plot a to produce the time series in plot c. The least square quadratic trend (red) in plot b is removed to produce time series in plot d. Horizontal lines in bottom plots mark $\pm$ 1 standard deviation.

Other characteristics calculated for the deseasonalized, detrended TOA flux anomalies were the autocorrelation function (see Figure 4.6, center plot) and frequency spectra (Figure 4.6, right plot). The auto-correlation will give us an idea of the memory intrinsic in observations versus climate models. The autocorrelation function validates our use of subsequent 20-year periods as 'independent' realizations of possible observed periods because the 'decorrelation time', as defined by the time the autocorrelation function falls below the 95% line is almost always less than 20-years. We also computed a frequency spectra to look at whether the variability is operating on the same length scales, like ENSO cycles of 2-7 years. While we calculated these statistical characteristics for all models, we decided to focus on the standard deviation of TOA flux anomalies as the primary interannual variability metric.

Normalizing the standard deviation of TOA flux anomalies by the standard deviation in TAS anomalies gives us a measure of how large the TOA flux anomaly

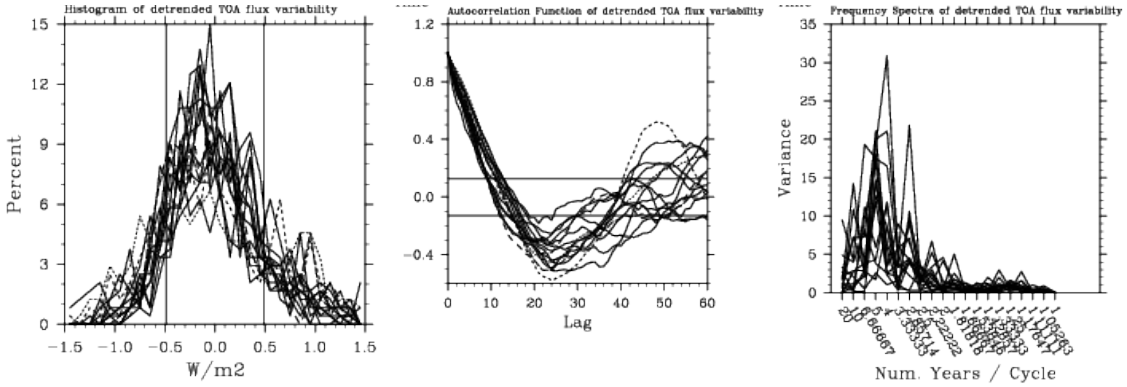

Figure 4.6: Example of various statistical characteristics calculated for the interannual time scale. The 20-year time slices are shown here from CM21. Plot a is a histogram of de-trended TOA flux anomalies; vertical lines mark the average standard deviation. Plot b is the autocorrelation function. Plot c is the frequency spectra.

variability is compared to the TAS variability, but it does not give us information about how the TOA flux anomalies and TAS anomalies vary together. For this reason, we use the standard deviation of detrended TOA flux anomalies as the interannual metric in units of Wm^{-2}.

Decadal

The decadal variability is characterized by 20-year and 100-year trends. The trend used in subsequent analyses and comparisons is defined as the slope of the least square linear regression line and is in units of Wm^{-2} per month and converted to Wm^{-2} per century. Alternatively, for the 100-year period, since a linear trend does not best fit the data, the trend is also calculated as the difference between the first and last 10-year averages and has units of Wm^{-2}. We normalize the long-term trends by dividing by the corresponding trend in the deseasonalized surface air temperature anomalies.

4.5 Regressions

We have separated and characterized the variability in the top of the atmosphere radiative flux anomalies due to water vapor, atmospheric temperature and surface albedo into the seasonal cycle, trend, and de-trended flux anomalies. It is useful to note that we can reconstruct the original time series with these three components,

though the trend from the 100-year runs used for the trend comparisons is different from the trend subtracted out in the interannual analysis. In total, this thesis considers 21 metrics of variability per feedback variable:

- 20-year seasonal amplitude (global, NH, SH) – 3 total
- 20-year standard deviation (global, NH, SH) – 3 total
- 20-year least squares linear trend (global, NH, SH) – 3 total
- 100-year seasonal amplitude (global, NH, SH) – 3 total
- 100-year standard deviation (global, NH, SH) – 3 total
- 100-year least squares linear trend (global, NH, SH) – 3 total
- 100-year end minus beginning trend (global, NH, SH) – 3 total

The regression coefficient and significance of each pair of variables are calculated in three ways. The first way (method 1) is by using each model ensemble member as an independent point in the analysis with the assumption that each ensemble member has the same uncertainty. There are thirteen models and each model has a set of ensemble members ranging from 1 to 9. In total, there are 44 ensemble members included in the analysis. When comparing two 100-year metrics, the fact that each of the 44 ensemble members are given equal weight could introduce some biases in the regressions, because models with more ensemble members will have more points in the analysis (i.e. more votes). When comparing two 20-year metrics, there are five 20-year sections for each 100-year ensemble member, resulting in 220 independent points in the analysis. Like before, the ensemble members aren't independent, nor are the five 20-year sections within an ensemble member really independent. However, the five sections could be considered independent realizations of a twenty year snapshot of the Earth's climate, since the autocorrelation function of the entire 100-year time series indicates a decorrelation time of less than 20 years. See Figure 4.6, plot b, bottom center. When comparing a 20-year and a 100-year metric, the five 20-year sections of each 100-year ensemble member are ensemble averaged resulting in 44 points in the analysis. Significance of the regression coefficient is determined by the p-value for a two-tailed student-t test using a t-statistic and degrees of freedom (number of points less 2) of the regression line and tested against the null hypothesis that the regression coefficient is zero (the metrics are unrelated, $H_0 = 0$). This regression on all points is indicated by the dashed line in result figures in the following chapter.

The second way (method 2) of calculating the regression coefficient and significance of a pair of metrics is by using an average value for each model (13 points) with the same regression analysis described in the previous paragraph. Again, we assume each model average has the same uncertainty (variance). For the 100-year metrics, the average is taken across the ensemble members for each model. For the 20-year metrics, the average is taken across all 20-year sections covering all ensemble members for each model (the number of values being averaged for each model is the number of ensemble members multiplied by five). This regression on 13 points is indicated by the solid line in result figures in the following chapter.

However, each model has a spread of values across ensemble members and 20-year sections. Since there is variance in both the x and y data, we ideally want to weight each average model value by the variance in both dimensions when computing the linear regression coefficient for the 13 model points. To account for the spread of the 20-year sections in the calculation of linear regressions, regression coefficients were computed a third way (method 3) by attaching weights to each model based on the inverse of the variance of the data. Of the significant regression coefficients, there is little difference ($\approx$10%) between the unweighted (method 2) and weighted regressions. For the purpose of this thesis, we focus on results for the regression coefficient and significance of the unweighted regressions. Results for the weighted regression are occasionally noted when very different from the unweighted regressions.

Chapter 5

Results

This thesis compares the variability of top of the atmosphere flux anomalies due to three variables (water vapor, atmospheric temperature, and surface albedo) over two time lengths (20 years and 100 years) in three geographic regions (global, northern hemisphere, and southern hemisphere) in thirteen global climate models. The variability is characterized on three time scales: annual, interannual, and decadal trends. A goal of this thesis is to test how well any information about variability in the TOA flux anomalies (due to individual variables) obtained from a short record, analogous to the length of the observed record, is related to variability in TOA flux anomalies and feedbacks obtained from a long record.

A metric has been computed for each combination of variables, time periods, geographic locations, and models in each of the time scales of interest: annual (amplitude of the global-averaged seasonal cycle of the feedback variable), interannual (standard deviation of global averaged TOA flux anomalies), and decadal (trends of global average TOA flux anomalies and feedbacks). All possible combinations of metrics are compared resulting in 210 total comparisons. However, we focus on those comparisons that are pertinent to determining any relationships between short-term (20-year) and long-term (100-year) variability. Each of the nine 20-year metrics are compared with each of the twelve 100-year metrics, resulting in 108 possible combinations of metrics. These metrics are compared by performing a least squares linear regression of each metric on every other metric and computing the significance of the regression coefficient. Then, metrics within a variable are compared across time scales and periods by using a least squares linear regression of pairs of metrics from each model.

This approach uses the 13 models as an ensemble to test for any short-term to long-term relationships within models as relates to the first research goal addressing the nature of variability in TOA flux anomalies between short and long time scales.

Then observational values of short-term variability are compared to corresponding short-term modeled variability as relates to my second research goal addressing the constraint of modeled variability of TOA flux anomalies by observations. Of most interest are any relationships in measurements of variability found between the 20-year period and 100-year period.

First, I will present results indicating that the two ways in which the 100-year trends are calculated are virtually equivalent (Section 5.1). Then each of the following sections presents results for each variable of the following short-term and long-term metric comparisons: 20-year trend with 100-year trend (Section 5.2), 20-year interannual variability with 100-year interannual variability (Section 5.3), 20-year seasonal amplitude with 100-year seasonal amplitude (Section 5.4), 20-year interannual variability with 100-year trend (Section 5.5), and 20-year seasonal amplitude with 100-year trend (Section 5.6). Section 5.7 presents results of the water vapor, atmospheric temperature, and surface albedo feedbacks calculated by regressing TOA flux anomalies onto surface air temperature anomalies.

5.1 100-year Trend Calculation

There are two ways that the 100-year trend in TOA flux anomalies is calculated. The first is a least squares linear trend (method 1); the second uses the difference between 10-year averages at the beginning and end of the 100-year period (method 2). The 'method 2' trend, is in units of Wm^{-2} calculated over 90 years. By using 10-year averages at the beginning and end of the time series, we are essentially decreasing the length of the series by 5 years at either end. We multiply this trend by a factor of 10/9 to produce an equivalent trend over 100 years. Figures 5.1, 5.2, and 5.3 show that there is very good correspondence between the two methods of trend calculation, but the trends calculated by 'method 1' tend to be slightly larger than the 'method 2' trends. The blue line marks the one-to-one correspondence between the two trend calculation methods. For water vapor (Figure 5.1) and atmospheric temperature (Figure 5.2) TOA flux anomalies, the 'method 1' trend is about 1.12 times larger in magnitude than the 'method 2' trend. For albedo (Figure 5.3), the 'method 1' trend is about 1.15 times larger than 'method 2' trend. The standard error for these regression coefficients is about 0.03, so the coefficients are not very different. Figures 5.1 and 5.2 show that for water vapor and atmospheric temperature, as the magnitude of the trend increases, the difference between the two trend calculation

methods becomes larger. If the models were ranked according to the size of the difference between the two methods, we'd see a very similar ranking for water vapor and atmospheric temperature. For example, CGCMT47 and CGCMT63 show the largest trend and discrepancy between methods in both water vapor and atmospheric temperature figures. Those models that have a large discrepancy between trend calculation methods also are less described by a linear fit with respect to time. That is, the time series of global TOA flux anomalies increases (decreases) non-linearly for water vapor (atmospheric temperature). For example, see plot b in Figure 4.5.

All models behave as expected with trends in water vapor and atmospheric temperature TOA flux anomalies consistent with climate warming (i.e. water vapor increases, decrease OLR and cause warming; atmospheric temperature increases, increase OLR and cause cooling). However, two models have negative trends in surface albedo TOA flux anomalies. A negative surface albedo TOA flux anomaly trend indicates that there is actually an increase in albedo and cooling over the century. This is inconsistent with a warming climate. Those same models also appear to be farther from the one-to-one line than the models with positive trends. By converting feedback variable anomalies into TOA effects, we can compare the magnitude of the trend in TOA effects among feedback variables. For water vapor, the range of trends among these 13 climate models is about 0.7 to 2.5 $Wm^{-2}century^{-1}$ with an average of around 1.3 $Wm^{-2}century^{-1}$. The approximate mean and range for atmospheric temperature is -2.0 $Wm^{-2}century^{-1}$ (-0.85 to -4.0); for surface albedo is 0.12 $Wm^{-2}century^{-1}$ (-0.1 to 0.35).

Even if the time series of TOA flux anomalies is not described well by a linear fit, the least squares linear trend can still be used to describe the overall rate of change over the 100-year period. In subsequent comparisons of 20-year measures of variability with 100-year trends and feedbacks, the 100-year trend calculated by a least squares linear fit ('method 1') is used in the regressions. Results for regressions using trends calculated with the end and beginning difference ('method 2') are occasionally shown as well to indicate little dependence in the results on choice of trend calculation.

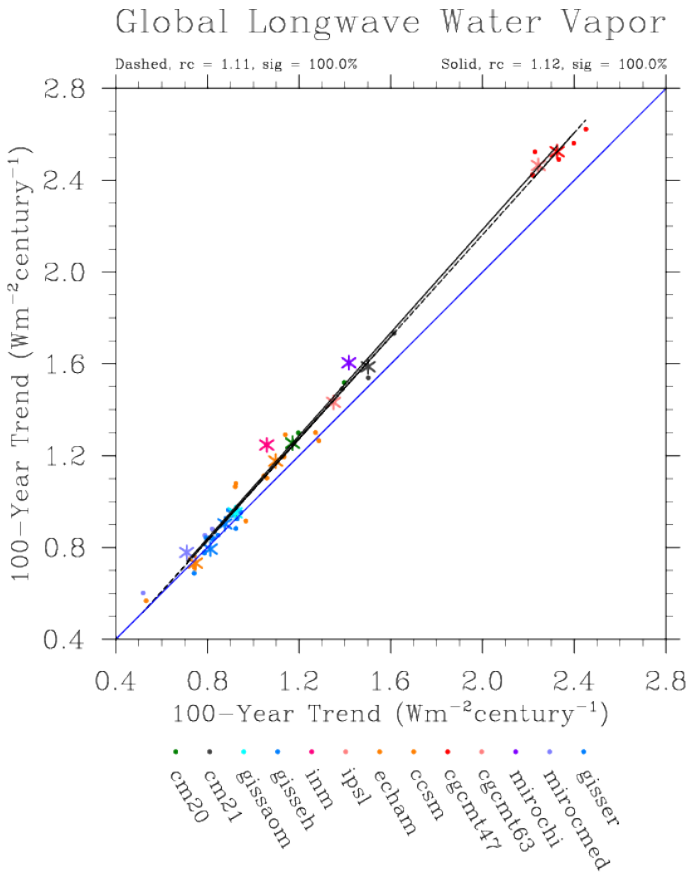

Figure 5.1: 100-year trend calculation comparison for LW water vapor TOA flux anomalies. The 'method 1' trend is on the Y-axis; the 'method 2' trend is on the X-axis. Each color represents a different climate model as indicated in the legend below the graph. Each dot refers to one ensemble member. The stars indicate the model average of all ensemble members (i.e. same colored dots). The blue line marks the one-to-one correspondence. The regression coefficient and significance of non-zero slope are given at the top of the plot for all dots (dashed) and all stars (solid).

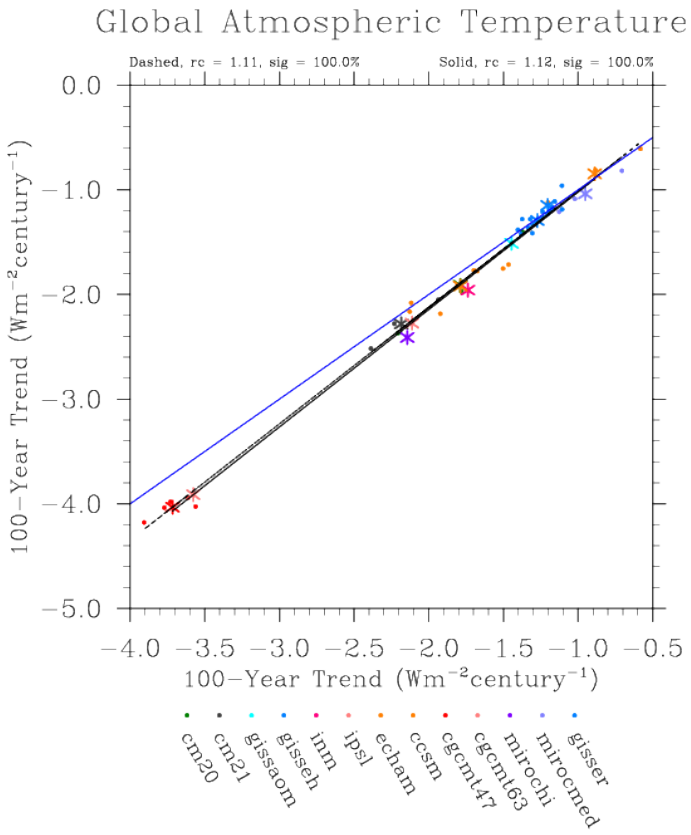

Figure 5.2: 100-year trend calculation comparison for atmospheric temperature TOA flux anomalies. As in Figure 5.1, 'method 1' trend is on the Y-axis and 'method 2' trend is on the X-axis.

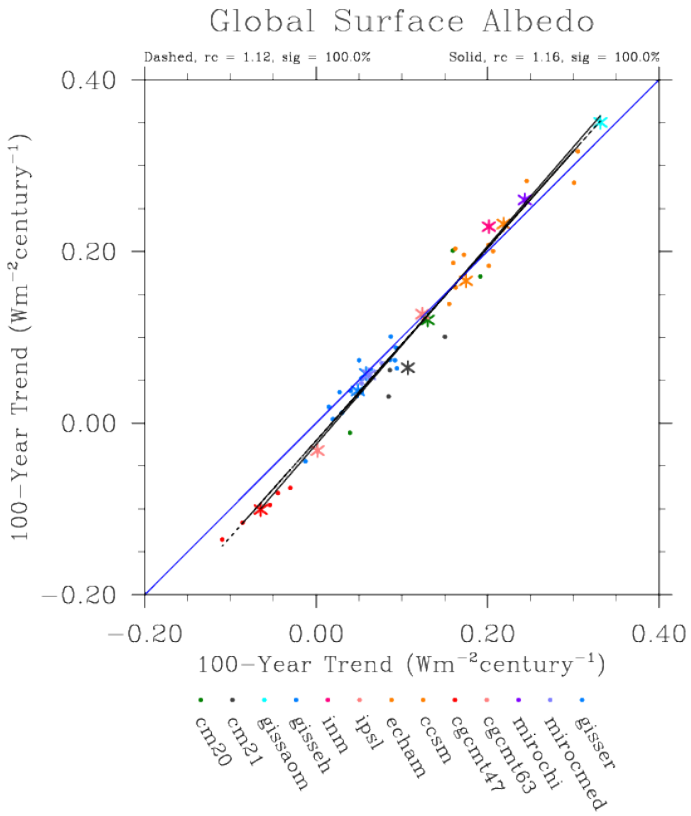

Figure 5.3: 100-year trend calculation comparison for surface albedo TOA flux anomalies. As in Figure 5.1, 'method 1' trend is on the Y-axis and 'method 2' trend is on the X-axis.

5.2 20-year Trend vs. 100-year Trend

In this framework, if 20 years were long enough to give information about a trend over a longer period, there should be a relationship between average 20-year trend and 100-year trend. In fact, there is a significant relationships between the average 20-year trends and the 100-year trends for all variables and almost all geographic locations (Figures 5.4 through 5.8). We expect this to be the case, especially if enough 20-year points are included, such that an ensemble of 20-year trends converges to the 100-year trend. However, it is of interest to ask how many 20-year points are enough to determine a 100-year trend. Do we find a relationship between one 20-year trend from each model and the subsequent 100-year trend? Because of the spread in the 20-year trends, some 20-year trends will be closer to the 100-year trend than

others. A measure of the 20-year spread is the ensemble average of the standard deviation divided by the mean. This gives the standard deviation as a percent of the mean and represents how well one 20-year period can be used to represent the mean 20-year periods used in subsequent analysis to estimate 100-year feedbacks. For water vapor, the percent standard deviation of the mean is 94.7%; for atmospheric temperature, 100.6%; for surface albedo, 163.9%. Because these values are close to 100% or over indicates that trends are not a good metric with which to constrain long-term feedbacks. Figures 5.4 through 5.8 show that one 20-year trend in TOA flux anomalies, similar to what we can currently calculate from satellite or reanalysis observations, cannot give us a confident estimate of the longer trend. The blue line on the following figures indicates the one-to-one correspondence of the average 20-year trend and the 100-year trend.

However, the average 20-year trends are not 'converging' to the 100-year trend because the regression slope is less than one. This might mean that by deseasonalizing each 20-year period and calculating a linear trend separately, we are excluding some information about the entire period. Most of the average 20-year trend values are actually larger than the average 100-year trend values resulting in a positive, non-zero y-intercept. This indicates that even for a 100-year period without an overall trend, the ensemble average of 20-year trends can still be positive.

Water vapor

In the case of water vapor TOA flux anomalies (Figure 5.4), the 100-year trend is always positive for all ensemble members of all models. This is consistent with the warming that occurs in all models over the 20^{th} century. However, there are some (9) individual 20-year sections within the 100-year records that have a negative trend. If modeled variability is similar to observed variability in TOA flux anomalies due to water vapor, with only 20 years, it cannot necessarily be confirmed that the trend in water vapor TOA flux anomalies is representative of 100-year trends, even though only $\approx 4\%$ of the 20-year trends are negative. We don't expect every 20-year trend to match up with the 100-year trend because climate change isn't linear. The 20-year trend in water vapor TOA flux anomalies in the reanalysis is weakly positive at $\approx 0.06\ Wm^{-2}century^{-1}$ (vertical black line in figure). The 100-year trends in models range from 0.57 to 2.62 $Wm^{-2}century^{-1}$, but almost all model simulations include 20-year periods with a similar trend magnitude as the reanalysis 20-year trend. Thus,

it would be difficult, by observational constraint, to further narrow what the 100-year trend in water vapor TOA flux anomalies might be.

The general relationship of large 20-year trends implying a large 100-year trend is significant with 99.7% confidence, but the relationship is not one-to-one. On average, the 20-year trends are larger in magnitude than the 100-year trends, although that is not necessarily the case when looking at one model individually. For example, the average 20-year trend in IPSL is smaller than the 100-year trend. The results presented above are for the 100-year trend calculated using 'method 1', that of a linear least squares trend. When using trends calculated by 'method 2', the slope of the regression decreases slightly (from 0.67 to 0.56), and the significance decreases slightly by $\approx 0.3\%$. There is a significant relationship using either trend calculation method.

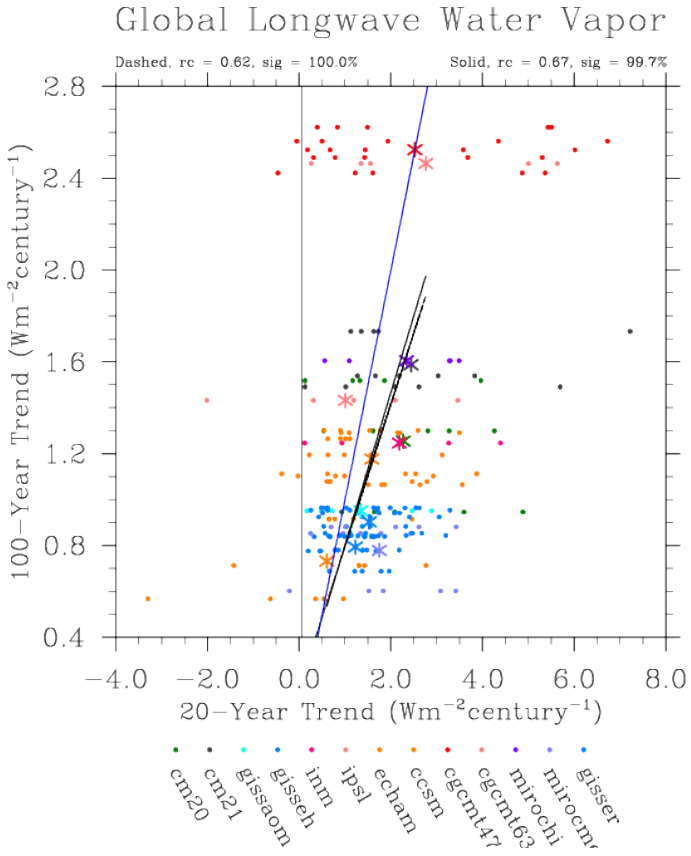

Figure 5.4: 20-year trend vs. 100-year trend for global average longwave water vapor TOA flux anomalies calculated by 'method 1'. Reanalysis value is indicated by the vertical black line.

Atmospheric Temperature

Globally (Figure 5.5) and in the NH and SH (not shown), the average 20-year trends are significantly and positively related to the 100-year trends. All 100-year trends in TOA flux anomalies are negative. A negative trend in the TOA effect of atmospheric temperature indicates that more energy is escaping the system due to higher atmospheric temperatures and increased emission. Most 20-year trends are negative; however, ten (less than 5%) 20-year periods have a positive trend, indicating a cooling of the atmosphere and reduction of OLR. The 20-year trend in atmospheric temperature TOA flux anomalies in the reanalysis is negative at $\approx$ -3.7 $Wm^{-2}century^{-1}$ (vertical black line in figure). Again, all models include 20-year trends spanning this value so the 100-year trend in TOA flux anomalies due to atmospheric temperature, which ranges from -0.61 to -4.18 $Wm^{-2}century^{-1}$, is difficult to constrain with the reanalysis observations. Like in the water vapor TOA flux anomaly trends, CGCMT47 and CGCMT63 are outliers with noticeably larger 100-year trends than the rest of the models. The northern and southern hemispheres plots look very similar to the global plot. Also, average 20-year trends are larger in magnitude than 100-year trends.

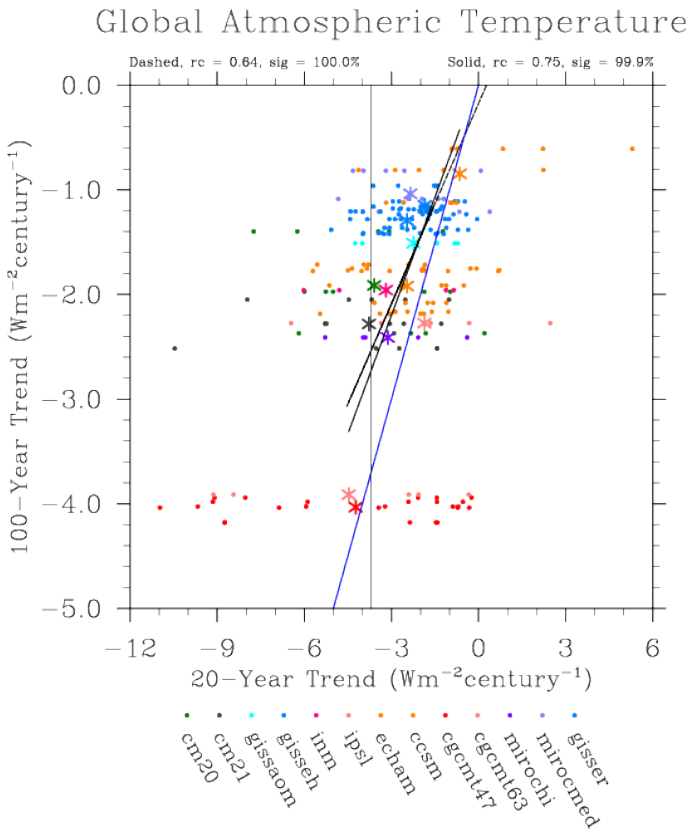

Figure 5.5: 20-year trend vs. 100-year trend for global average atmospheric temperature TOA flux anomalies calculated by 'method 1'. Reanalysis value indicated by vertical black line.

Surface Albedo

Globally and in the northern hemisphere, the average 20-year trends in albedo are significantly, positively related to the respective 100-year trend, but not the southern hemisphere. Globally (Figure 5.6), the regression coefficient is 0.84 (99.8% significance). In the northern hemisphere (Figure 5.7), the regression coefficient is 0.79 (99.9% significance). In the southern hemisphere (Figure 5.8), the regression coefficient is 0.27, but not significant (69%). The northern hemisphere shows a stronger relationship between 20-year and 100-year trends than in the SH. In the global and NH averages, while the general relationship between 20-year and 100-year trends is positive (i.e. big 20-year trend = big 100-year trend), there are many individual 20-year trends that are negative for a positive 100-year trend, though we don't expect

all the 20-year trends to match the 100-year trend if the 100-year trend is changing (i.e. nonlinear). In fact, $\approx$ 30% of the 20-year periods have a negative trend for simulations where the 100-year trends are positive. A similar percentage is seen for the NH (32%) and SH (36%). In the southern hemisphere, average 20-year trends can be either positive or negative for models with positive 100-year trends. It is interesting to note that not all models produce positive 100-year trends. CGCMT47 and CGCMT63 both have a negative 100-year trend, globally and in the NH, with both positive and negative 20-year trends. In the SH, CGCMT47 and CGCMT63 have positive SH trends. Also, the ordering of 100-year trends in the NH and SH is not the same suggesting that there isn't a unified process occurring in both hemispheres. Most of the average 20-year trends are more positive than the 100-year trend as evident by their position below the one-to-one line. The 20-year trend in surface albedo TOA flux anomalies in the reanalysis is negative at $\approx$ -0.26 $Wm^{-2}century^{-1}$ (vertical black line in figure). Most models include 20-year trends around this value and some models do show some larger negative 20-year trends. Using the 'method 2' trend instead of the 'method 1' trend slightly improves the one-to-one relationship, but the difference is within the standard error of the fit; the significance remains over 99%.

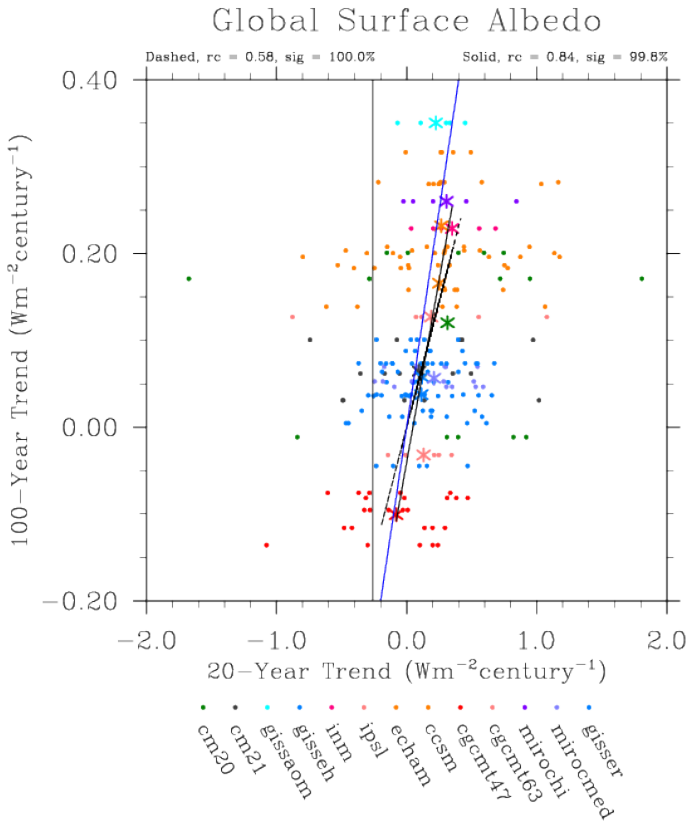

Figure 5.6: 20-year trend vs. 100-year trend for global average surface albedo TOA flux anomalies calculated by ‘’method 1’.

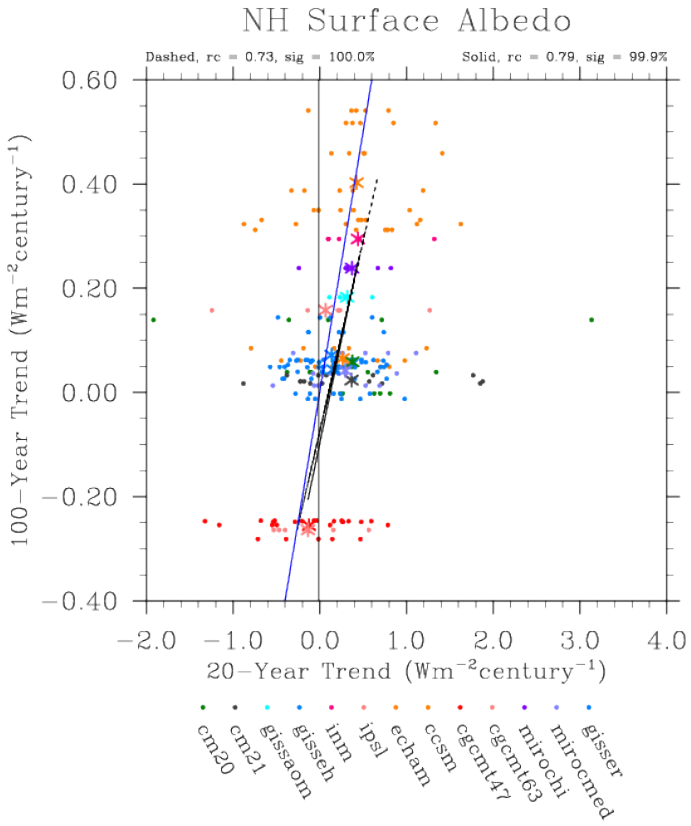

Figure 5.7: 20-year trend vs. 100-year trend for surface albedo northern hemisphere average TOA flux anomalies calculated by 'method 1'.

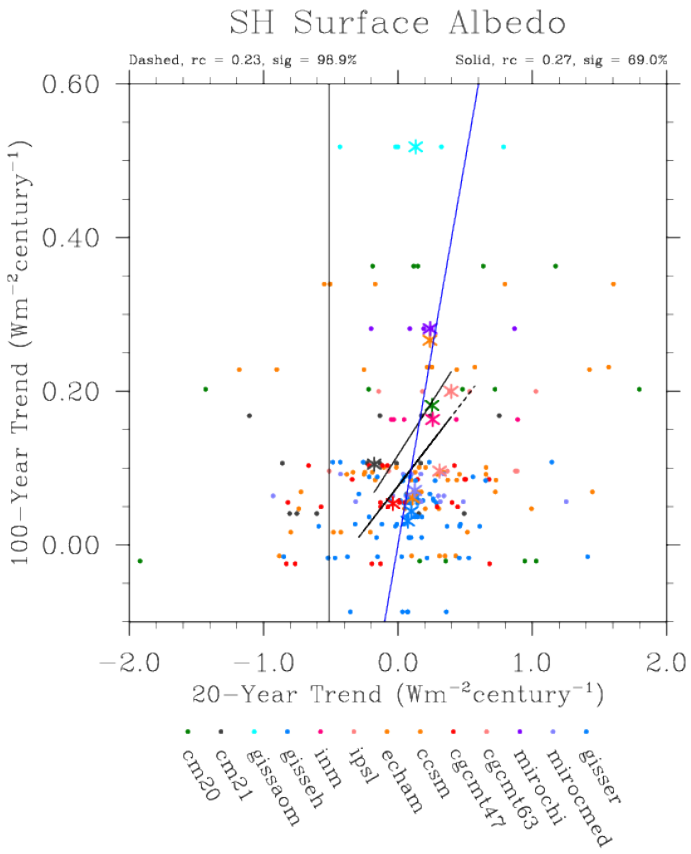

Figure 5.8: 20-year trend vs. 100-year trend for surface albedo southern hemisphere average TOA flux anomalies calculated by 'method 1'.

Discussion points

A general observation across all variables is that the average 20-year trends tend to be larger than the 100-year trends as is evident by the values lying below (or above for atmospheric temperature) the one-to-one line. However, this is not necessarily the case for an individual model. The slope of the global average surface albedo regression is closest to the one-to-one relationship between 20-year trends and 100-year trends with a slope of 0.84. The slope of the water vapor and atmospheric temperature regressions are 0.67 and 0.75, respectively. However, the y-intercept of all these regression lines is non-zero. The systematic underestimation of the 100-year trend by the average 20-year trend could be due to non-linear behavior of the time series and how the records were divided to calculate individual 20-year trends.

5.3 20-year Interannual Variability vs. 100-year Interannual Variability

Table 5.1 lists regression slopes and significances from comparisons of average 20-year standard deviation of TOA flux anomalies and 100-year standard deviation. There is good agreement between the two time periods indicating that the distribution of anomalies sampled in 20-years is similar to the distribution of anomalies over 100-years. Though in general, the 20-year standard deviations are smaller than the 100-year standard deviations because there may be some extreme anomalies or cycles that occur over longer periods that aren't captured in 20-years. Any difference in standard deviation due to sample size is not important because n is large for both the 20-year and 100-year periods. The ensemble average percent standard deviation of the mean for all of these 20-year values over the global average is 12.7% for water vapor, 13.3% for atmospheric temperature, and 9.3% for surface albedo.

Table 5.1: Regression slopes and significance between 20-year standard deviation and 100-year standard deviation of TOA flux anomalies for all three variables and regions. Normalized regressions and significances are shown in parenthesis.

Var	TA	TA	WVLW	WVLW	AL	AL
Region	Slope	Sig (%)	Slope	Sig (%)	Slope	Sig (%)
GL	0.99 (1.08)	100 (100)	0.99 (1.01)	100 (100)	0.87 (0.86)	100 (100)
NH	0.98 (1.07)	100 (100)	0.98 (1.00)	100 (100)	0.94 (1.01)	100 (100)
SH	1.00 (1.05)	100 (100)	0.99 (1.01)	100 (100)	0.73 (0.70)	100 (100)

The values outside the parenthesis refer to the regression coefficients and significance levels for the 20-year to 100-year standard deviation comparison. The values within parenthesis are the comparisons of the normalized standard deviations. Normalization of the standard deviation is done by dividing by the standard deviation in the detrended surface air temperature time series. Normalizing in this way gives information about how much the TOA flux anomalies vary with reference to how much the surface air temperature varies. Notice that the relationship is changed very little and agree mostly within the standard error.

Surface Albedo

Overall, the average 20-year standard deviations tend to be smaller than the 100-year standard deviations, although there are some individual 20-year periods with larger standard deviation than the 100-year period. These 20-year periods are seen below the blue one-to-one line in Figure 5.9. As the magnitude of the standard deviation increases there appears to be more spread between the 20-year periods. The NH shows the closest one-to-one relationship, followed by global, then SH (right columns in Table 5.1). The reanalysis 20-year standard deviation is 0.079 globally, 0.099 in NH, and 0.118 in SH.

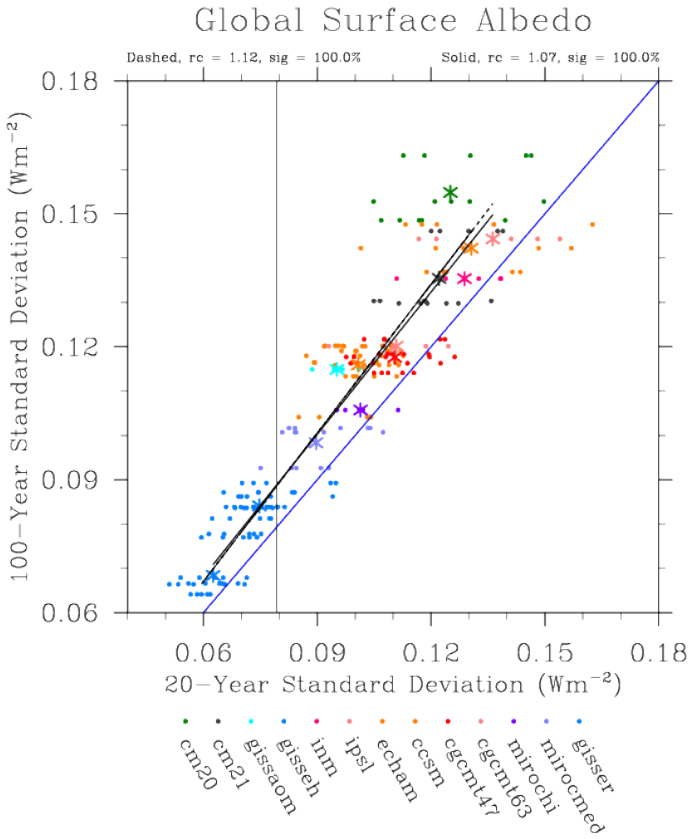

Figure 5.9: 20-year standard deviation with 100-year standard deviation for global average surface albedo TOA flux anomalies. Reanalysis value indicated by vertical black line.

Water Vapor & Atmospheric Temperature

The relationship between standard deviation of 20-year and 100-year periods is essentially one-to-one for global, NH and SH regions. To a lesser degree than albedo, the spread of 20-year periods increases with standard deviation magnitude. There does not appear to be much difference in the relationships of the three regions. This is so for atmospheric temperature too. The reanalysis 20-year standard deviation for water vapor is 0.303 globally, 0.35 in NH, and 0.414 in SH. The reanalysis 20-year standard deviation for atmospheric temperature is 0.503 globally, 0.593 in the NH, and 0.524 in the SH. These reanalysis values fall within the range of climate model standard deviations of TOA flux anomalies with some models better matching the reanalysis than others. This means that given a relationship in the models between the 20-year standard deviation and the 100-year feedback, then the reanalysis observations might be used to constrain the 100-year feedback.

5.4 20-year Seasonal Amplitude vs. 100-year Seasonal Amplitude

It should be that the average 20-year seasonal cycle amplitudes are related essentially one-to-one to the 100-year seasonal cycle amplitudes because of how the seasonal cycle for each period is defined. See Table 5.2 for regression coefficients of 20-year seasonal amplitudes with 100-year seasonal amplitudes for all three variables and regions.

Table 5.2: Regression slopes and significance for 20-year seasonal amplitudes with 100-year seasonal amplitude for all three variables and regions. Regressions and significances for normalized amplitudes are given in parenthesis.

Var	TA	TA	WVLW	WVLW	AL	AL
Region	Slope	Sig (%)	Slope	Sig (%)	Slope	Sig (%)
GL	0.99 (0.88)	100 (100)	1.06 (1.07)	100 (100)	0.97 (0.88)	100 (100)
NH	1.00 (1.00)	100 (100)	1.00 (1.00)	100 (100)	1.00 (1.00)	100 (100)
SH	1.00 (0.98)	100 (100)	1.01 (0.98)	100 (100)	0.99 (0.850)	100 (100)

The following figures (5.10, 5.11, & 5.13) show the 20-year seasonal amplitude regressed onto the 100-year seasonal amplitude for the northern hemisphere for surface albedo, water vapor and atmospheric temperature. The global and SH figures (not

shown) are essentially the same (or within the standard error) except for the global water vapor shown in Figure 5.12. The 20-year global seasonal amplitudes for water vapor are slightly larger than the 100-year global amplitudes (Figure 5.12). This may be due to the fact that we use the seasonal cycle of the natural log of specific humidity instead of specific humidity itself.

The reanalysis surface albedo seasonal amplitude for the northern hemisphere is 3.2% (vertical black line in Figure 5.10). In the southern hemisphere, the reanalysis albedo seasonal amplitude is 1% and globally is 1.1%. It is of note that the reanalysis surface albedo seasonal amplitude is much smaller in magnitude than the amplitude in almost all of the models. The water vapor seasonal amplitude in the reanalysis is 0.184 globally, 0.781 in NH, and 0.444 in SH. The atmospheric seasonal amplitude in the reanalysis is 2.786 globally, 10.358 in NH, and -4.785 in SH. Table 5.3 gives the range of 20-year seasonal amplitudes for climate models for each variable and region.

Table 5.3: ERA-Interim reanalysis seasonal amplitude values (column 2) for all variables and regions with the minimum (column 3) and maximum (column 4) modeled 20-year seasonal amplitudes.

Albedo	ERA	Min	Max
Global	0.011	0.018	0.052
NH	-0.032	-0.084	-0.035
SH	0.01	-0.002	0.070
LW Water Vapor	ERA	Min	Max
Global	0.184	0.097	0.248
NH	0.781	0.565	0.886
SH	0.444	0.359	0.571
Atm Temp	ERA	Min	Max
Global	2.786 K	1.884 K	3.410 K
NH	10.358 K	8.481 K	11.578 K
SH	-4.785 K	-7.07 K	-3.919 K

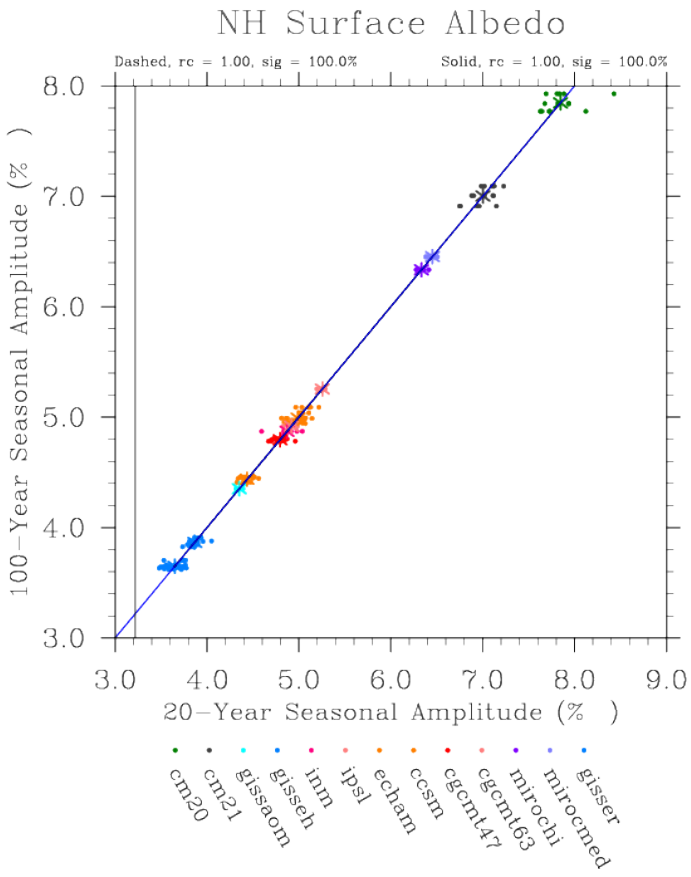

Figure 5.10: 20-year seasonal amplitude vs. 100-year seasonal amplitude for NH surface albedo TOA flux anomalies. Note that all lines are essentially on the one-to-one line (blue).

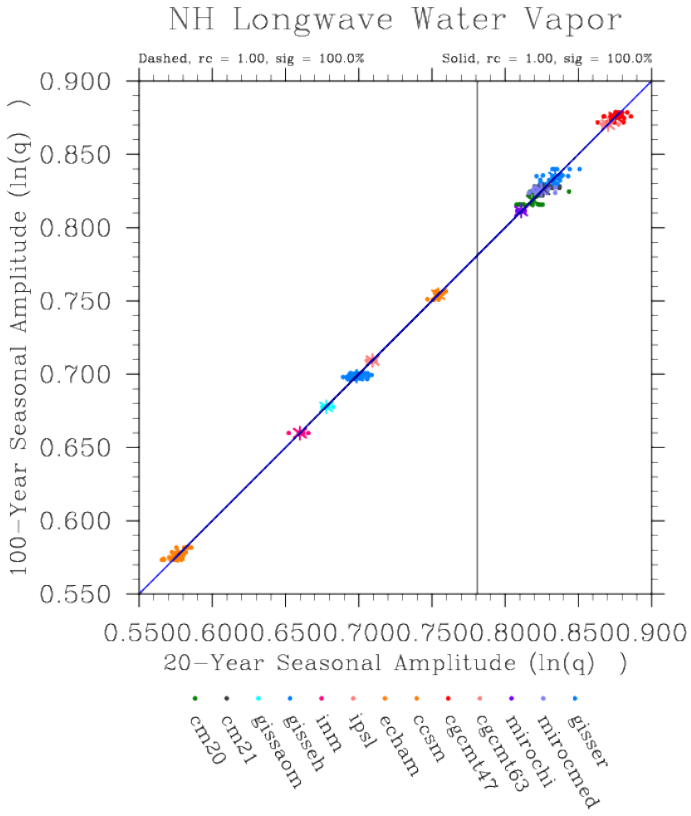

Figure 5.11: 20-year seasonal amplitude vs. 100-year seasonal amplitude for NH LW water vapor TOA flux anomalies.

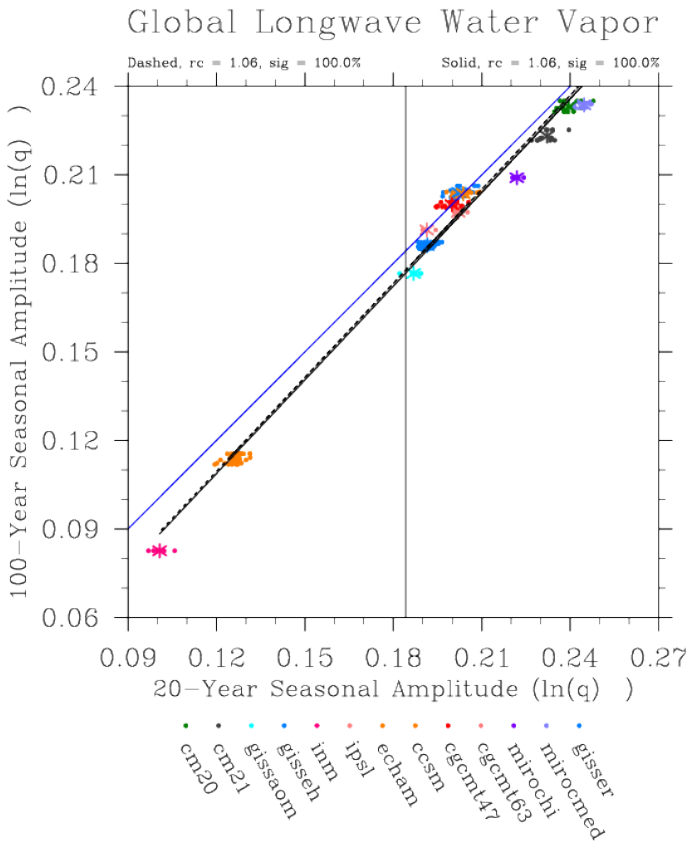

Figure 5.12: 20-year seasonal amplitude vs. 100-year seasonal amplitude for global LW water vapor TOA flux anomalies.

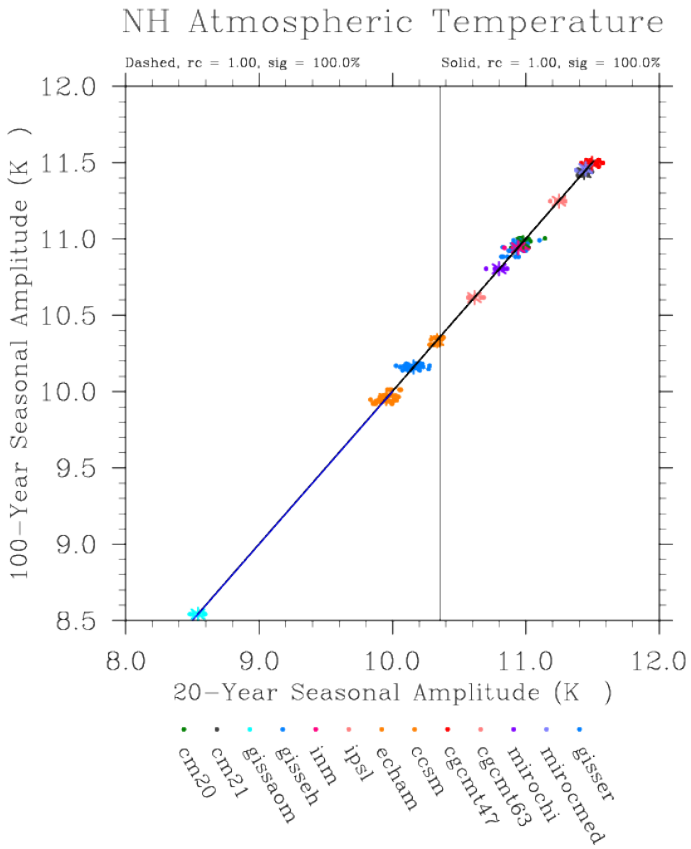

Figure 5.13: 20-year seasonal amplitude vs. 100-year seasonal amplitude for NH atmospheric temperature TOA flux anomalies.

It is worthwhile to note that the ordering of models are different for all three variables. Models with large atmospheric temperature cycle don't always have large water vapor cycles and vice versa. For example, GISSAOM has the smallest NH atmospheric temperature seasonal amplitude while a different model has the smallest NH LW water vapor seasonal cycle. Another example is INM, which has the second smallest NH water vapor amplitude and is among the largest NH atmospheric temperature seasonal amplitude. Because each of the models is essentially distinct, with regard to seasonal cycle amplitudes, we can easily identify short-term model performance compared to the reanalysis observations. However, this does not indicate that the same models will perform similarly with respect to long-term feedbacks. The ensemble average percent standard deviation of the mean for global annual cycle amplitude is 1.5% for water vapor, 1.2% for atmospheric temperature, and 1.4% for

surface albedo. This close clustering of points within each model, in addition to the model separation, suggest that the seasonal amplitude is essentially constant with time. While the mean state may change over time, this suggests that one 20-year period can be used to represent the mean of 20-year periods which is used in subsequent analysis to estimate 100-year feedbacks. The annual cycle amplitude may be a good metric to constrain long-term feedbacks.

5.5 20-year Interannual Variability vs. 100-year Trend

Surface Albedo

There is a significant relationship between the 20-year standard deviation in TOA flux anomalies due to albedo and the 100-year trend for the southern hemisphere (Figure 5.14). The northern hemisphere and global domains do not show a significant relationship (not shown). In the SH, the regression slope is 1.66 with a significance of 98.2%. The y-intercept of the regression slope is not at zero because even with no 100-year trend, we would still expect there to be natural interannual variability in these flux anomalies. The weighted and unweighted regression slopes in this case are quite different, so taking account of the variance in the standard deviation is important, though only the unweighted regression is presented for consistency. Regressing 20-year standard deviation on to 100-year trend calculated with 'method 2' instead of 'method 1', results in a ≈ 20 % change in the regression slope and slight increase in significance.

When normalizing by the standard deviation of the surface air temperature and comparing with the normalized 100-year trend, or feedback, (Figure 5.15) we see that the regression slope is 0.42 and the slope seems to depend on the inclusion of a few models that sample higher standard deviations and feedbacks. The normalized standard deviation is a measure of the variability of TOA flux anomalies compared to the variability of surface air temperature anomalies. The reanalysis SH surface albedo TOA flux anomaly normalized standard deviation is 0.84 Wm^{-2}. When using the reanalysis and the regression relationship in Figure 5.15 to estimate the 100-year feedback, the value and error range is 0.21 (0.027 to 0.44) $Wm^{-2}K^{-1}$. There is little difference when using the normalized trend (feedback) calculated with 'method 1' instead. The error in the regression slope and y-intercept is included, as well as the spread of the 20-year values. The reanalysis observations are assumed to be 'perfect'.

The inclusion of its error would widen the estimates. The estimates presented here, then, are best case estimates. Though the error range is smaller than the range of models, there is substantial overlap among the models. The range of models within the observation bounds is larger than the estimated range. The bounds on the observations come from the spread in the modeled 20-year values. This overlap makes it more difficult to estimate long-term feedbacks from 20-year normalized standard deviation. It is similarly so for non-normalized standard deviation (not shown) with an estimate and range of 0.20 (0.013 to 0.42) $Wm^{-2}K^{-1}$.

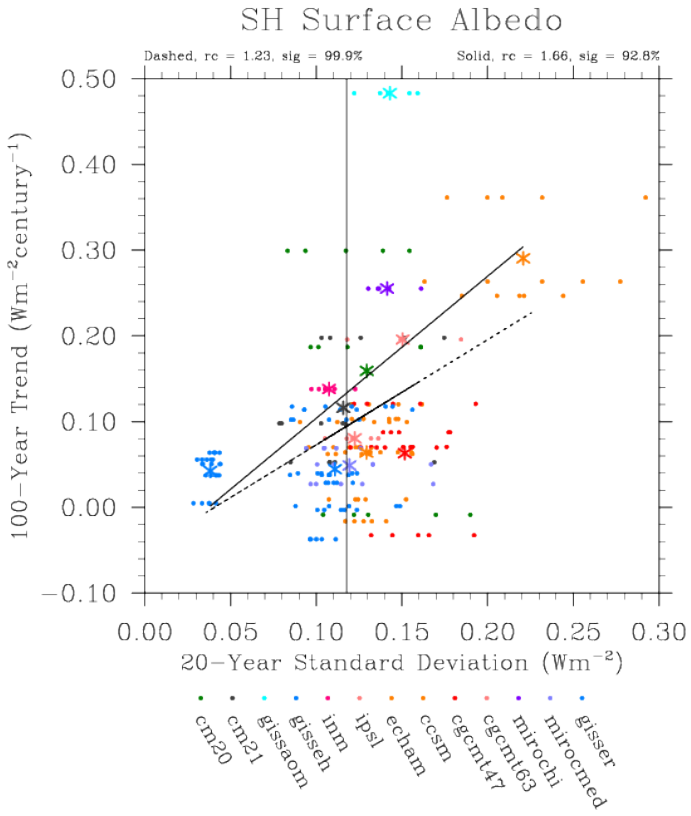

Figure 5.14: 20-year standard deviation vs. 100-year trend for SH surface albedo TOA flux anomalies. Trend calculated by 'method 2'.

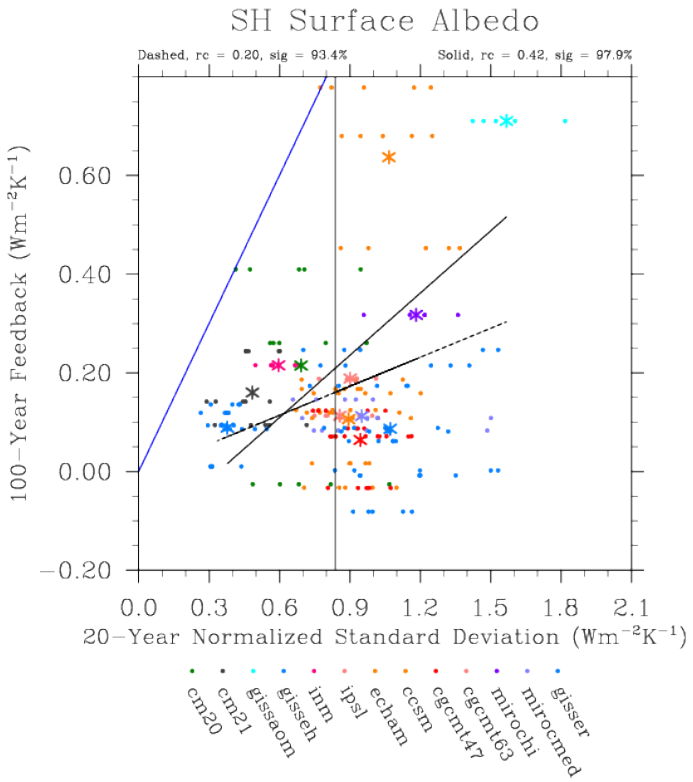

Figure 5.15: 20-year normalized standard deviation vs. 100-year feedback (normalized trend calculated by 'method 2') for SH surface albedo TOA flux anomalies. Reanalysis value indicated by vertical black line.

Atmospheric Temperature & Water Vapor

There are not any significant relationships between 20-year standard deviation and 100-year trends for neither atmospheric temperature nor water vapor. This may indicate that some factors that contribute to the natural variability of the atmospheric temperature and water vapor are not related to factors contributing to the overall increasing temperature (e.g. ENSO and sensible and latent heat). The lack of relationships between interannual variability and trends in both atmospheric temperature and water vapor TOA effects is probably due to their close anti-correlation. Table 5.4 shows the regression slopes and significance for 20-year standard deviations with 100-year trends for surface albedo, atmospheric temperature, and water vapor TOA flux anomalies over global, NH and SH domains.

Table 5.4: Regression slopes and significance for 20-year standard deviation and 100-year trends calculated by 'method 1'. Values in parenthesis correspond to regressions of normalized standard deviations with feedbacks (i.e. normalized trends).

Var	TA	TA	WVLW	WVLW	AL	AL
Region	Slope	Sig (%)	Slope	Sig (%)	Slope	Sig (%)
GL	1.46 (0.18)	67.4 (58.1)	-0.53 (0.08)	28.8 (29.4)	0.64 (0.21)	28.8 (48.6)
NH	1.79 (0.05)	70.1 (11.9)	-0.33 (0.44)	16.5 (80.9)	0.61 (-0.25)	38.8 (49.4)
SH	1.10 (0.34)	56.4 (91.8)	-0.03 (-0.10)	1.9 (39.6)	1.55 (0.41)	88 (98)

There is a significant relationship between the 20-year normalized standard deviation and the 100-year normalized trend (feedback) in the SH for atmospheric temperature (Figure 5.16). The reanalysis normalized SH standard deviation is 3.73 $Wm^{-2}K^{-1}$. The corresponding 100-year feedback estimate is -6.66 (-1.79 to -3.43) $Wm^{-2}K^{-1}$. There is also a significant relationship (91.4%) between the 20-year normalized standard deviation and the 100-year feedback in the NH for water vapor (Figure 5.17). The reanalysis normalized NH standard deviation is 1.76 $Wm^{-2}K^{-1}$. The corresponding 100-year feedback estimate is 1.58 (1.08 to 2.15) $Wm^{-2}K^{-1}$.

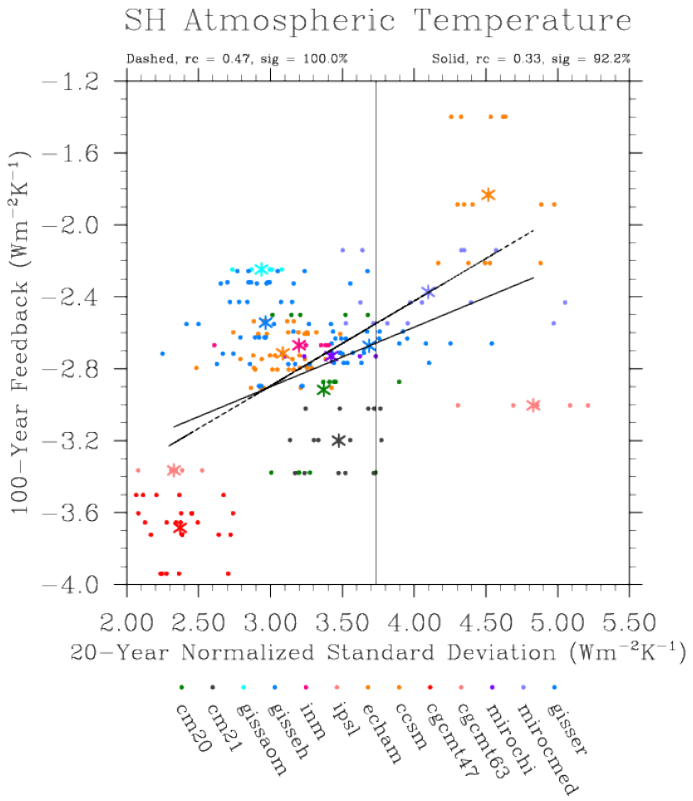

Figure 5.16: Regression between 20-year normalized standard deviation and 100-year feedback calculated with trend method 2 for the southern hemisphere atmospheric temperature TOA flux anomalies. Reanalysis value indicated by vertical black line.

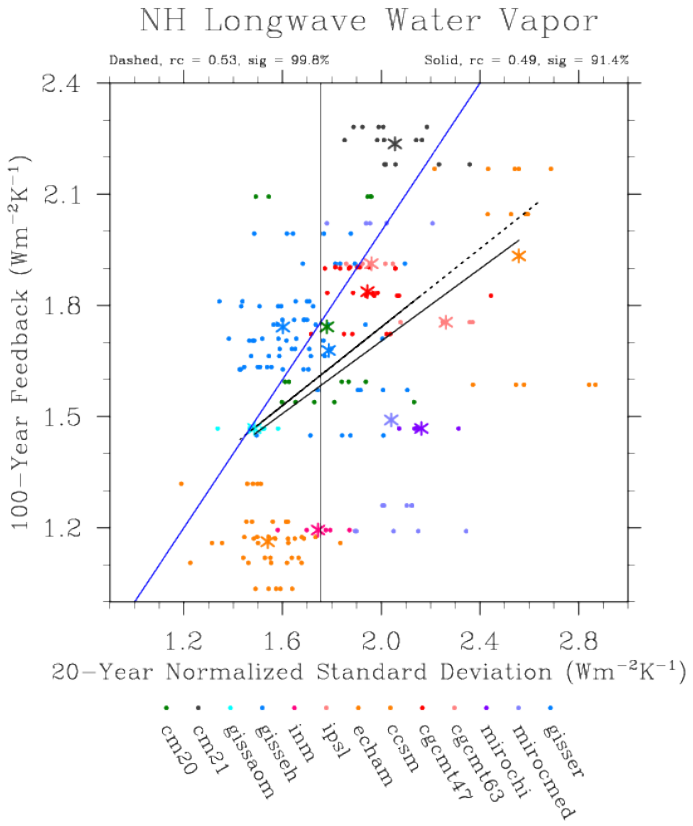

Figure 5.17: Regression between 20-year normalized standard deviation and 100-year feedback calculated with trend method 2 for the northern hemisphere LW water vapor TOA flux anomalies. Reanalysis value indicated by vertical black line.

5.6 20-year Seasonal Variability vs. 100-year Trend

Surface Albedo

Because of previous work (i.e. Hall and Qu, 2006), we expected to find that intra-seasonal changes in surface albedo normalized by surface air temperature change are related to longer term changes such that we find a relationship between the seasonal cycle amplitude and the 100-year trend. Normalizing by surface air temperature changes is important for albedo changes because albedo changes are most closely related to temperature changes. In fact, the 20-year northern hemisphere normalized seasonal amplitude is significantly related to the 100-year global (not shown) and northern hemisphere (Figure 5.18) normalized trend, or feedback, when using

all data points. However, when using model averages, we do not find a significant relationship. The regression coefficient is in units of $(Wm^{-2}K^{-1})/(\%K^{-1})$ or simply $(Wm^{-2})/\%$. Furthermore, if we don't normalize the seasonal albedo change (and the 100-year trend) by the corresponding surface air temperature change, the relationship is insignificant.

On the other hand, the best relationship between 20-year seasonal amplitude and 100-year trends is in the southern hemisphere for the non-normalized seasonal amplitude and the normalized 100-year trend (i.e. feedback). See Figure 5.19. Why we see a relationship in the southern hemisphere with the non-normalized 20-year amplitude and we see a relationship in the northern hemisphere with the normalized 20-year amplitude can possibly be explained by the dominant processes in each hemisphere. In the northern hemisphere, there is more land area so snow cover changes over the season is an important process that is especially dependent on surface temperatures within a given season. The southern hemisphere is more dominated by sea ice changes which may depend more on the mean climate state and ocean temperatures than on the seasonal air temperature changes.

The reanalysis 20-year normalized seasonal NH amplitude is 0.57%, which is most consistent with GISSER & GISSEH. Their corresponding 100-year NH feedbacks are between ≈ 0.1 to 0.2 $Wm^{-2}K^{-1}$. However, several other models have similar 100-year feedbacks, but much larger seasonal amplitudes. Using 100-year feedbacks calculated using trend calculation 'method 2' slightly improves the significance though it remains a weak relationship. In the southern hemisphere, the reanalysis seasonal amplitude is 1.1%. Using the NH and SH amplitudes from the reanalysis and the respective regression relationships from Figures 5.18 and 5.19, the estimated 100-year feedbacks are 0.07 (-0.12 to 0.26) $Wm^{-2}K^{-1}$ for the northern hemisphere, and 0.37 (0.26 to 0.50) $Wm^{-2}K^{-1}$ for the southern hemisphere. However, since neither regression relationship is significant, long-term feedback constraint with this methodology for surface albedo is not very useful.

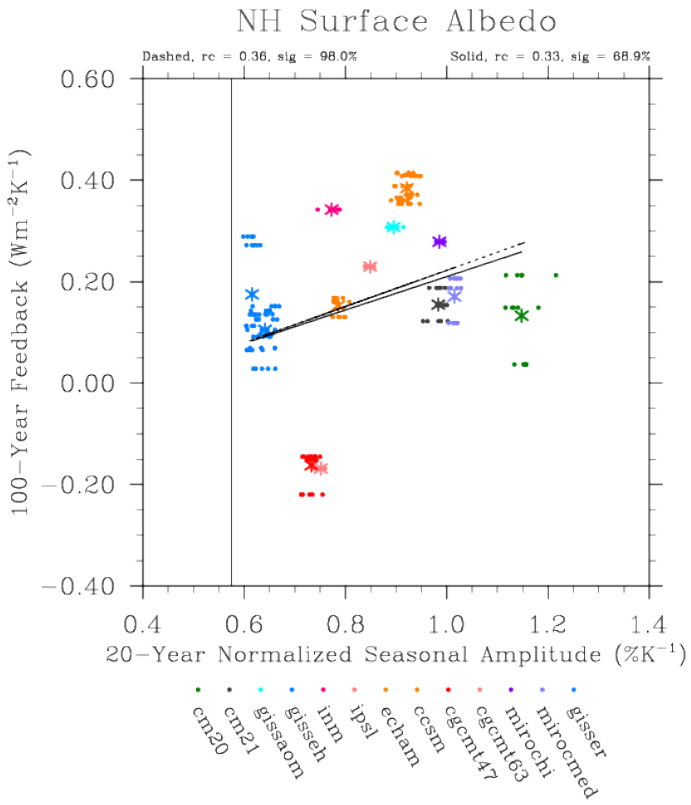

Figure 5.18: 20-year normalized seasonal amplitude vs. 100-year feedback for NH surface albedo TOA flux anomalies. Feedback trend calculated by 'method 2'.

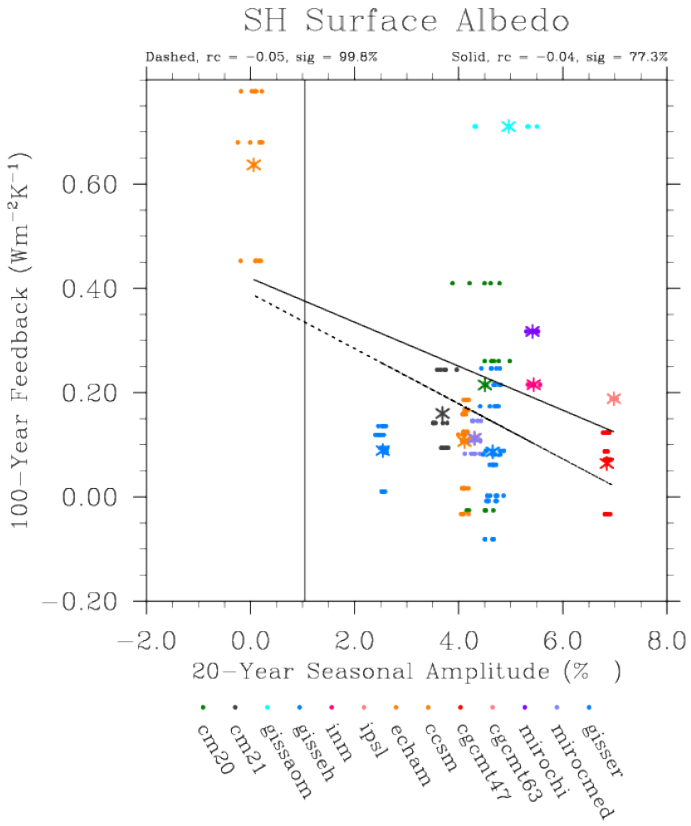

Figure 5.19: 20-year seasonal amplitude vs. 100-year feedback for SH surface albedo TOA flux anomalies. Feedback trend calculated by 'method 2'.

Atmospheric Temperature

Table 5.5 shows the regression slopes and significance for 20-year seasonal amplitude onto 100-year trend for global, NH and SH regions. Only the SH 20-year seasonal amplitude is significantly related to the 100-year SH trend as shown by the significance level in Figure 5.20. The seasonal amplitude is computed as the JJA-DJF so values are negative for the southern hemisphere because this is winter minus summer. The general relationship of increasing atmospheric temperature seasonal amplitude magnitude with increasing TOA flux trend magnitude is also seen in Table 5.5 for the NH and global domains, but of less significance. Regressing the seasonal amplitude on to the 100-year trend calculated by 'method 2' tends to weaken the significance, but the general relationship persists. The relationship between non-normalized 20-year seasonal amplitude and non-normalized 100-year TOA flux trends due to atmospheric

temperature anomalies depends on the inclusion of a few models that seem to be outliers, although these 'outliers' might not necessarily be outside the physically reasonable possible trajectories. CGCMT47 and CGCMT63 have the greatest 100-year trend and the greatest magnitude of seasonal amplitude. INM has a 100-year trend similar to the majority of models, but with a much higher seasonal amplitude.

The relationship between the 20-year seasonal amplitude and 100-year feedback for the NH, SH, and globe are shown in Table 5.5. The reanalysis 20-year SH seasonal amplitude is -4.78 K and falls within the realm of the majority of models. The reanalysis seasonal amplitude for the NH is 10.36 K and globally is 2.78 K. Using the SH reanalysis value and the relationship in Figure 5.21, the estimated SH feedbacks is -2.64 (-2.09 to -3.19) $Wm^{-2}K^{-1}$. The NH feedback estimate (not shown in figures) is -2.63 (-0.88 to -4.37) $Wm^{-2}K^{-1}$. Using 'method 2' trend calculation results in little difference.

Normalizing by the corresponding surface air temperature seasonal amplitude worsens the relationship. This comparison relates the seasonal amplitude of atmospheric temperature at 850 hPa and the net TOA effect of atmospheric temperature changes throughout the entire atmosphere. Normalizing the seasonal amplitude should result in a value close to one since the seasonal temperature change at 850 hPa would be very similar to that at the surface. If all 20-year normalized atmospheric temperature seasonal amplitudes are close to one, then the correlation with 100-year TOA flux anomaly trend would tell us something other than how the seasonal amplitude relates to the 100-year TOA flux trend. Instead it would tell us how the relative difference between the seasonal amplitude at 850 hPa versus that at the surface relates to the 100-year trend. If all models had a similar seasonal amplitude at 850 hPa and at the surface, the comparison with 100-year trend would essentially just show the range of 100-year trend values among the models. Figure 5.22 shows the normalized global atmospheric temperature seasonal amplitude regressed onto the normalized 100-year trend in TOA flux anomalies (i.e. feedbacks). It appears that the seasonal amplitude at 850 hPa is less than at the surface for all models, but that models tend to group in two areas: those models with almost equal 850 hPa and surface amplitudes, and those with a 850hPa seasonal amplitudes of $\approx 20\%$ less than the seasonal amplitude at the surface. Figure 5.22 seems to suggest a difference among models rather than an ensemble relationship.

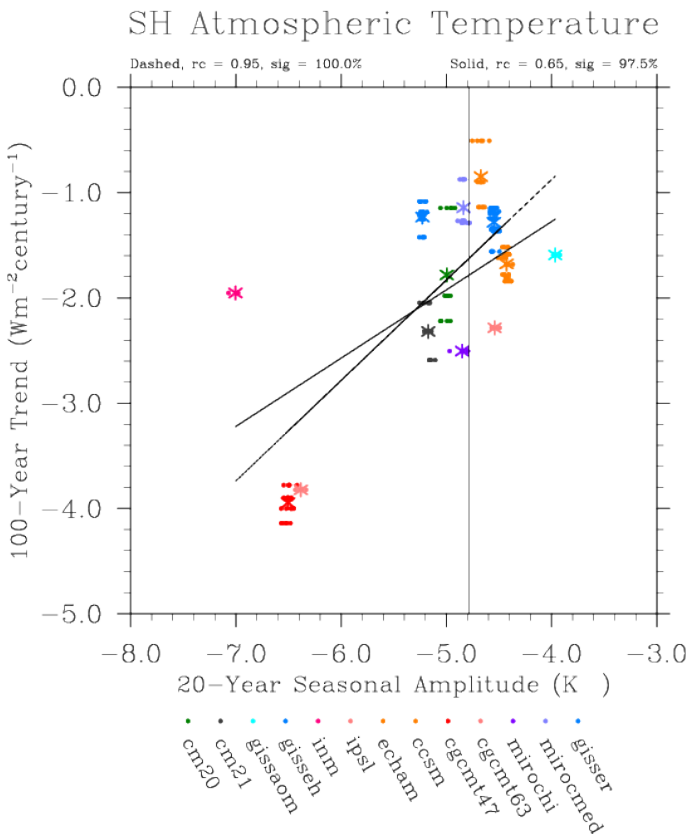

Figure 5.20: 20-year seasonal amplitude vs. 100-year trend for SH atmospheric temperature TOA flux anomalies. Note that CGCMT47 and CGCMT63 fall outside of the majority of models.

Table 5.5: Regression slopes and significance for 20-year seasonal amplitudes and 100-year trends for all three variables and regions. Values in parenthesis correspond to regressions and significances between 20-year seasonal amplitude and 100-year normalized trends (i.e. feedbacks).

Var	TA	TA	WVLW	WVLW	AL	AL
Region	Slope	Sig (%)	Slope	Sig (%)	Slope	Sig (%)
GL	0.81 (-0.09)	70 (18.6)	0.11 (4.02)	2 (96.2)	-0.01(-0.06)	25.8 (69.6)
NH	-0.49 (-0.35)	80.6 (94.7)	2.66 (2.51)	85.2 (98.7)	0.0 (-0.01)	5.7 (23.2)
SH	0.65 (0.30)	97.5 (94.3)	6.0 (2.76)	98.8 (98.2)	-0.0 (-0.04)	2 (74.8)

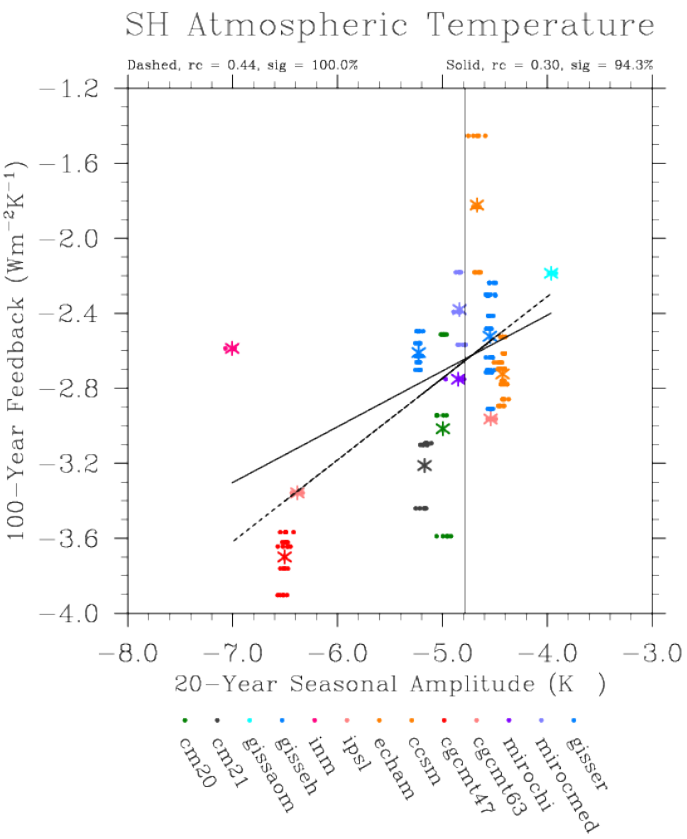

Figure 5.21: 20-year seasonal amplitude vs. 100-year feedback for SH atmospheric temperature TOA flux anomalies. Feedback trend calculated by 'method 1'.

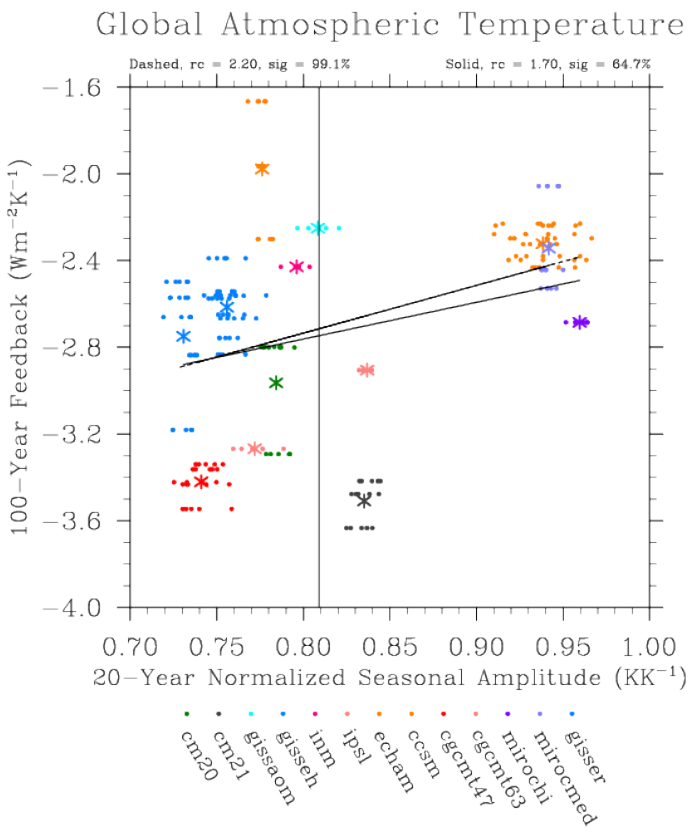

Figure 5.22: 20-year normalized global seasonal amplitude vs. 100-year global feedback for atmospheric temperature. Feedback trend calculated by 'method 1'.

Water Vapor

As seen from Table 5.5, there is no relationship between the global 20-year water vapor seasonal amplitude and global 100-year trend in TOA flux anomalies (Figure 5.23). The northern hemisphere dominates the global water vapor seasonal cycle, so it is no surprise that the NH seasonal amplitude versus trend plot (Figure 5.24) is similar to Figure 5.23 (global). The biggest difference is the stronger NH seasonal amplitude of CGCMT63 and CGCMT47, without which the relationship might not be there. The relationship between seasonal amplitude and 100-year trend is stronger in the southern hemisphere than in the northern hemisphere. For the SH (Figure 5.25), there is a significant positive relationship such that larger 20-year seasonal amplitudes correspond to larger trends in 100-year water vapor TOA flux anomalies. Even excluding CGCMT63 and CGCMT47, a relationship would appear to remain.

Notice that NH seasonal amplitudes are greater than in the SH. While seasonality is more pronounced in the NH, the relationship between seasonal amplitude and 100-year trends is stronger in the SH. This could be due to a larger ocean surface area in the SH. It could be that the global relationships are not significant because of the NH and SH are seasonally out of phase and taking a global average seasonal cycle combines information from opposite seasons. Regressing 20-year seasonal amplitude on to 100-year trend calculated by 'method 2' only reduces the significance of the relationship. Normalizing the seasonal amplitude by corresponding surface air temperature changes worsens the relationships, though we don't expect the natural log of water vapor to be linearly proportional to surface air temperature.

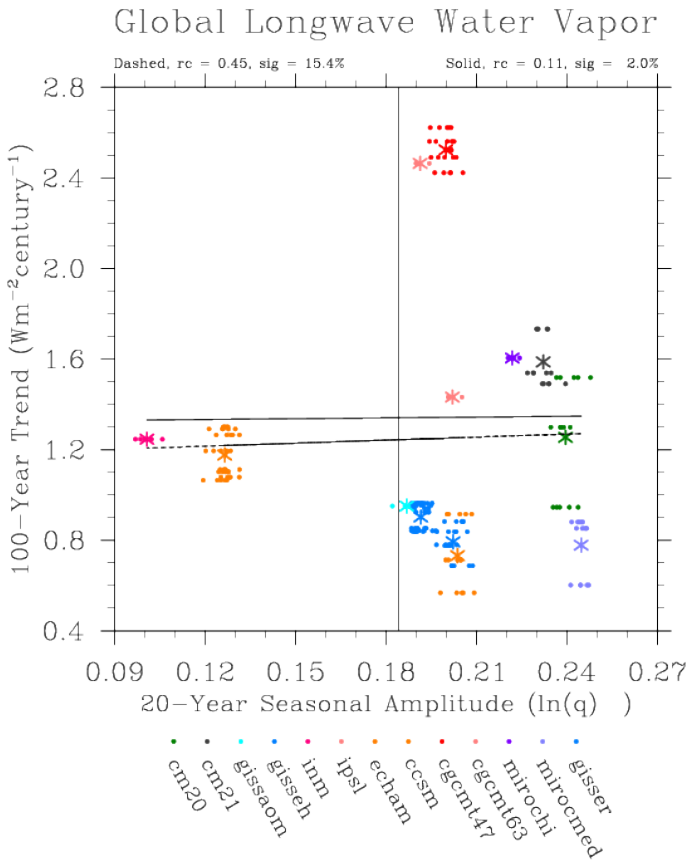

Figure 5.23: 20-year seasonal amplitude vs. 100-year trend for global average LW water vapor TOA flux anomalies. Trend calculated by 'method 1'.

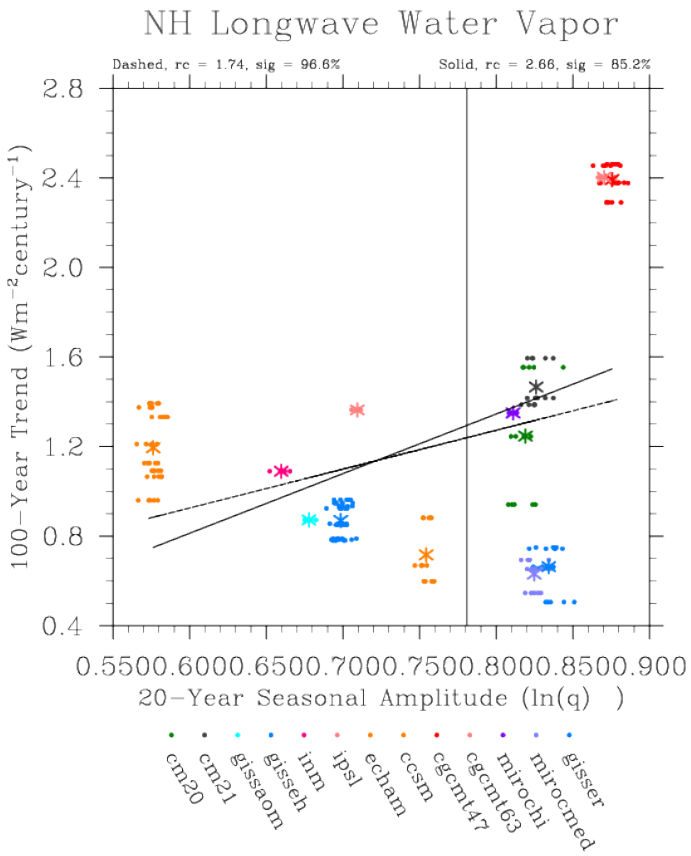

Figure 5.24: 20-year seasonal amplitude vs. 100-year trend for NH LW water vapor TOA flux anomalies. Trend calculated by 'method 1'.

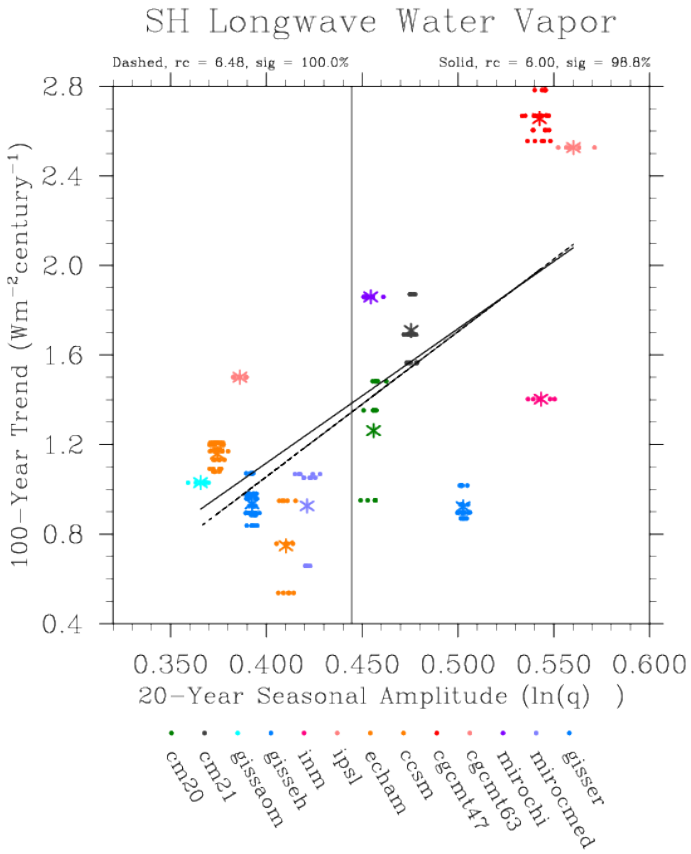

Figure 5.25: 20-year seasonal amplitude vs. 100-year trend for SH LW water vapor TOA flux anomalies. Trend calculated by 'method 1'.

Since atmospheric temperature and water vapor are closely coupled, it is not surprising that the significant relationships occur in the same region, the southern hemisphere. In the discussion section we expand on why we might see these relationships in the SH instead of in the NH where seasonality is more pronounced.

The regression of the 20-year seasonal amplitude with the 100-year feedback (i.e. normalized trend) is strongest for the northern and southern hemispheres. The global regression is weaker because the global seasonal amplitude is essentially a residual between the northern and southern hemisphere seasonal cycles since they are seasonally out of phase. The reanalysis 20-year seasonal amplitude of water vapor in the northern and southern hemispheres are 0.781 and 0.444, respectively, and are indicated by vertical black lines in the figures. Using the respective linear regression relationships in Figures 5.26 and 5.27, accounting for the standard error in slope and y-intercept,

the estimated feedbacks are 1.76 (1.09 to 2.44) $Wm^{-2}K^{-1}$ for the northern hemisphere and 1.96 (1.51 to 2.42) $Wm^{-2}K^{-1}$ for the southern hemisphere. Using the trend calculation 'method 2' instead yields similar results.

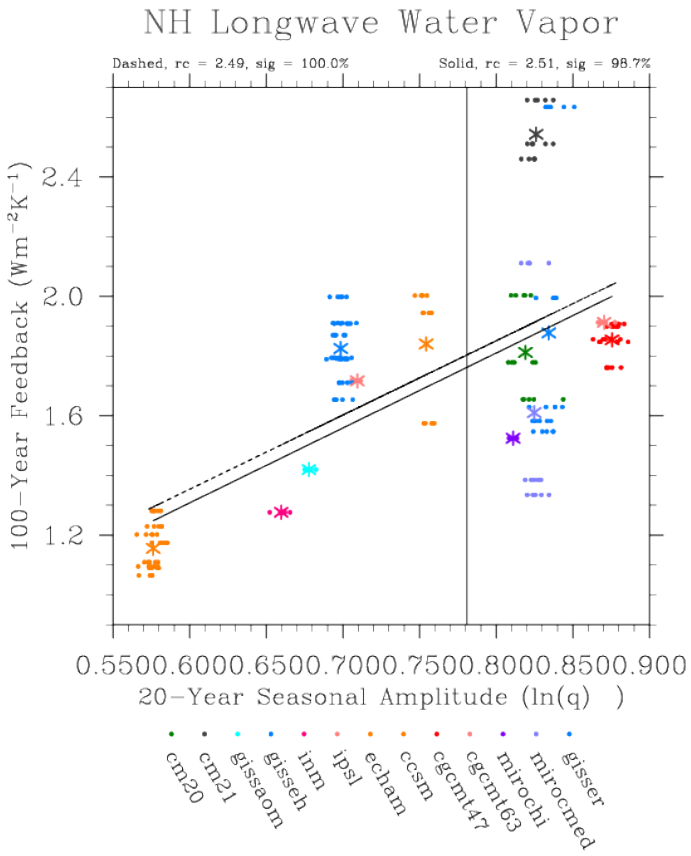

Figure 5.26: 20-year seasonal amplitude vs. 100-year feedback for NH LW water vapor TOA flux anomalies. Feedback trend calculated by 'method 1'. Reanalysis value indicated by vertical black line.

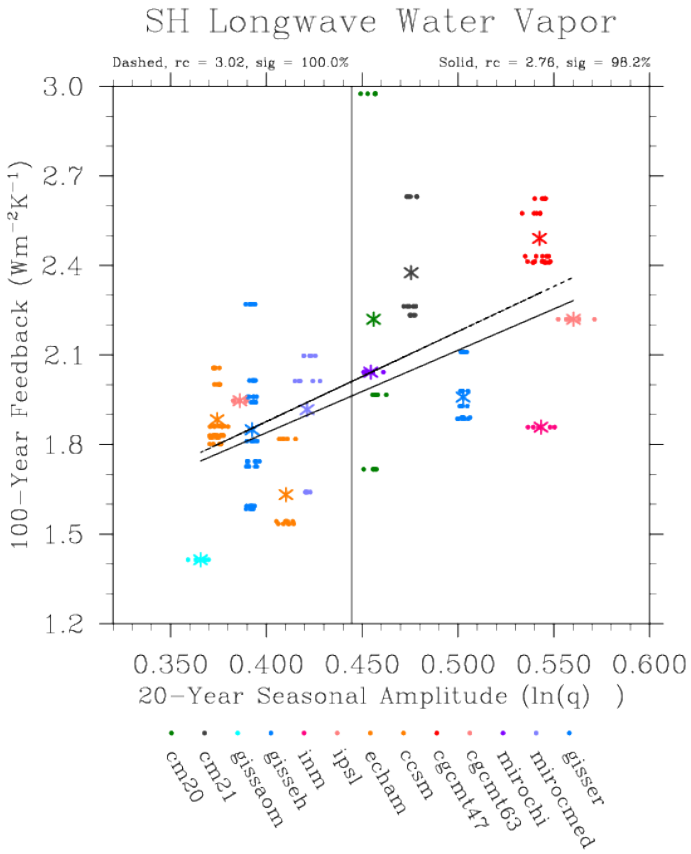

Figure 5.27: 20-year seasonal amplitude vs. 100-year feedback for SH LW water vapor TOA flux anomalies. Feedback trend calculated by 'method 1'. Reanalysis value indicated by vertical black line.

5.7 TOA Radiative Flux Anomalies and TAS regressions

Feedbacks associated with the transient 20^{th} century simulations for surface albedo, water vapor and atmospheric temperature were calculated another way using the method outlined by Gregory et al. (2004). That is, global TOA flux anomalies due to each of the three variables (calculated using the radiative kernel technique) over the 20^{th} century were regressed onto anomalies of global surface air temperature (TAS) over the same period for each ensemble member of each model. Table 5.6 lists the feedback values in $Wm^{-2}K^{-1}$. Figures 5.28, 5.29 and 5.30 are examples of the regressions for the three variables for one climate model, CCSM. All y-intercepts are essentially zero and the regressions for each ensemble member are not necessarily

within the standard error of each other. Feedbacks were calculated for the entire 20^{th} century as well as each individual 20-year period for each ensemble member of each models (not shown).

Table 5.6: 20^{th} century radiative feedbacks for atmospheric temperature (left column), long wave water vapor (middle column), and surface albedo (right column) calculated using the Gregory et al (2004) method. An ensemble mean, minimum and maximum value are given for each model. All values are in $Wm^{-2}K^{-1}$.

Model	Atm Temp	LW Water Vapor	Surface Albedo
CM20	-2.72 (-2.74 to -2.67)	1.61 (1.57 to 1.67)	0.26 (0.22 to 0.28)
CM21	-3.18 (-3.21 to -3.17)	1.98 (1.91 to 2.02)	0.17 (0.16 to 0.18)
GISSAOM	-2.19 (-2.19 to -2.19)	1.31 (1.31 to 1.31)	0.47 (0.47 to 0.47)
GISSEH	-2.49 (-2.67 to -2.34)	1.43 (1.22 to 1.61)	0.15 (0.11 to 0.18)
INM	-2.49 (-2.49 to -2.49)	1.60 (1.60 to 1.60)	0.27 (0.27 to 0.27)
IPSL	-3.07 (-3.07 to -3.07)	1.96 (1.96 to 1.96)	0.23 (0.23 to 0.23)
ECHAM	-3.31 (-3.53 to -3.14)	2.09 (2.02 to 2.21)	0.23 (0.18 to 0.26)
CCSM	-2.21 (-2.29 to -2.14)	1.28 (1.24 to 1.36)	0.27 (0.23 to 0.31)
CGCMt47	-3.24 (-3.32 to -3.14)	1.98 (1.88 to 2.04)	-0.04 (-0.06 to -0.01)
CGCMT63	-3.09 (-3.09 to -3.09)	1.91 (1.91 to 1.91)	0.02 (0.02 to 0.02)
MIROCHI	-2.60 (-2.60 to -2.60)	1.67 (1.67 to 1.67)	0.30 (0.30 to 0.30)
MIROCMED	-2.65 (-2.74 to -2.56)	1.75 (1.65 to 1.89)	0.18 (0.16 to 0.21)
GISSER	-2.32 (-2.38 to -2.21)	1.38 (1.33 to 1.44)	0.12 (0.04 to 0.16)

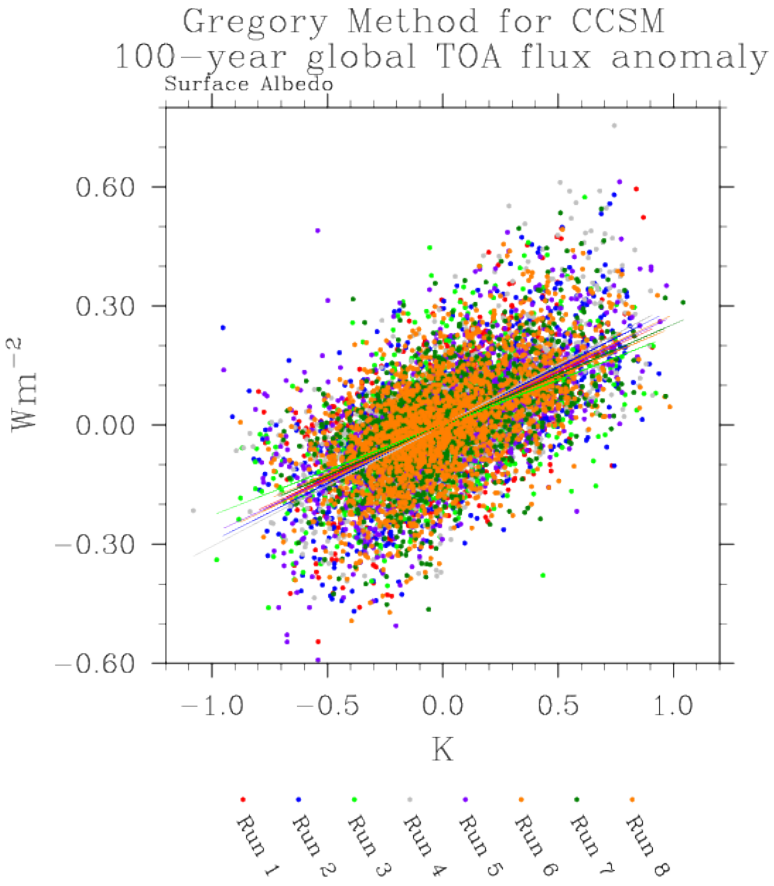

Figure 5.28: Example of surface albedo TOA flux anomaly regression with surface air temperature following Gregory et al. (2004). Each color represents a different ensemble member of CCSM, as indicated in the legend below the plot.

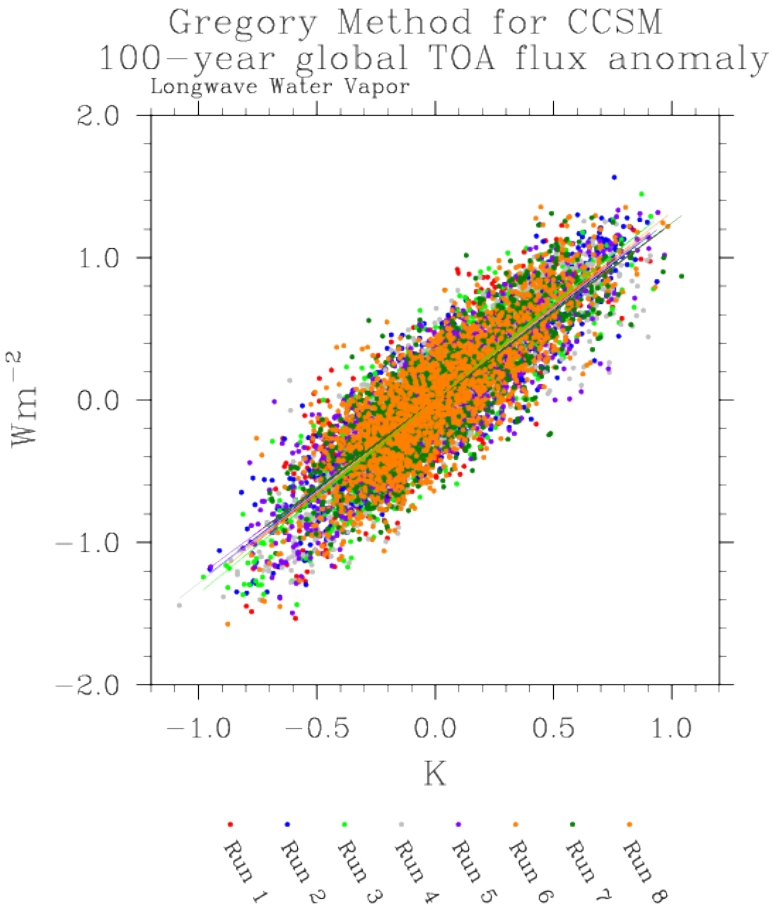

Figure 5.29: Same as Figure 5.28, but for LW water vapor.

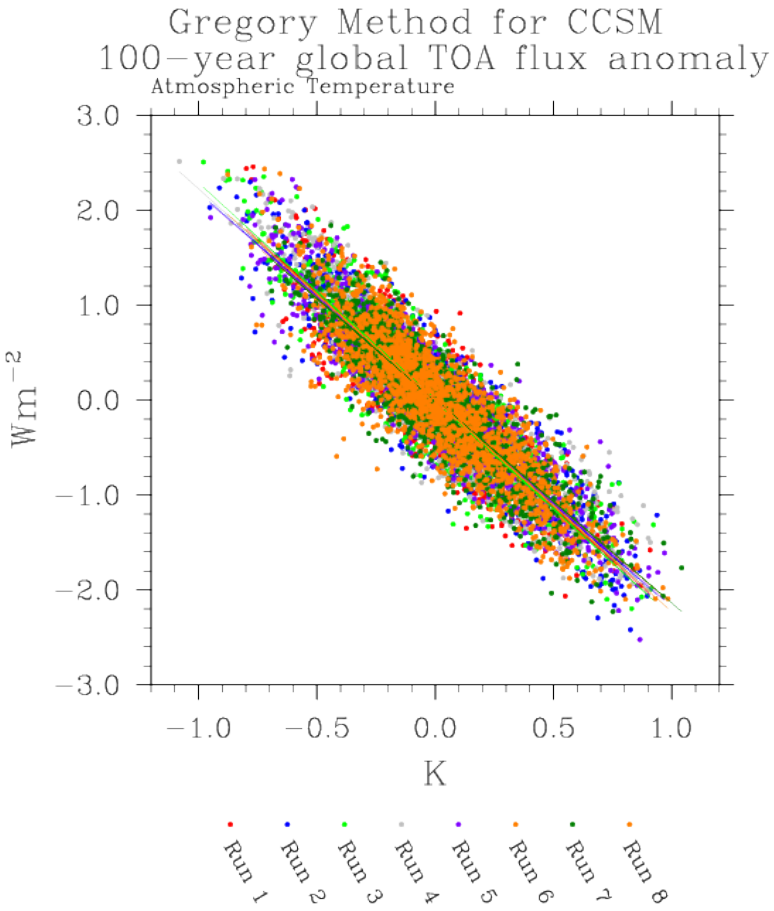

Figure 5.30: Same as Figure 5.28, but for atmospheric temperature.

In Figures 5.31, 5.32, and 5.33, global feedbacks derived from 20-year periods are regressed onto global feedbacks derived from 100-year periods. There is a large spread in the 20-year feedbacks, but significant non-zero relationships with 100-year feedbacks. The 20-year global surface albedo feedback is best related to the 100-year global feedback with a slope and significance of 1.21 and 99.6%. For water vapor, the regression slope is 0.38 with a significance of 98.9%. For atmospheric temperature, the regression slope is 0.41 with a significance of 98%. These results are simply presented as an intriguing extension of this work. Since the spread in the 20-year feedbacks is so large, it may not be very useful to try and estimate the 100-year feedbacks from 20-year observations. However, the correspondence between the 20-year and 100-year feedbacks using this method is encouraging. Further interpretation and analysis is reserved for future work.

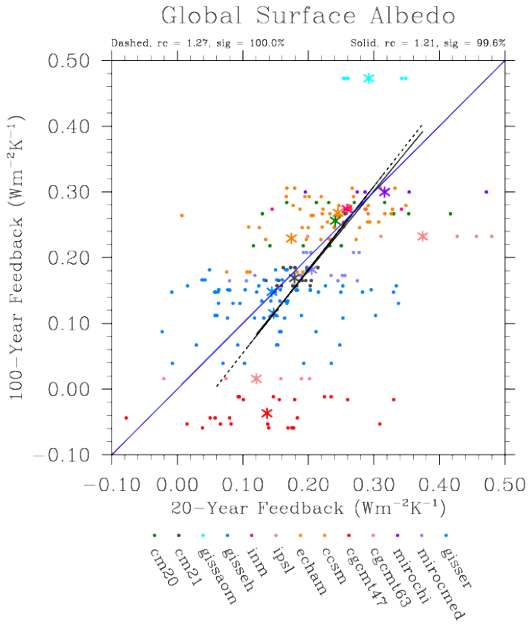

Figure 5.31: 20-year global feedbacks compared with 100-year global feedbacks for surface albedo as calculated with the RKT and Gregory et al. (2004) method.

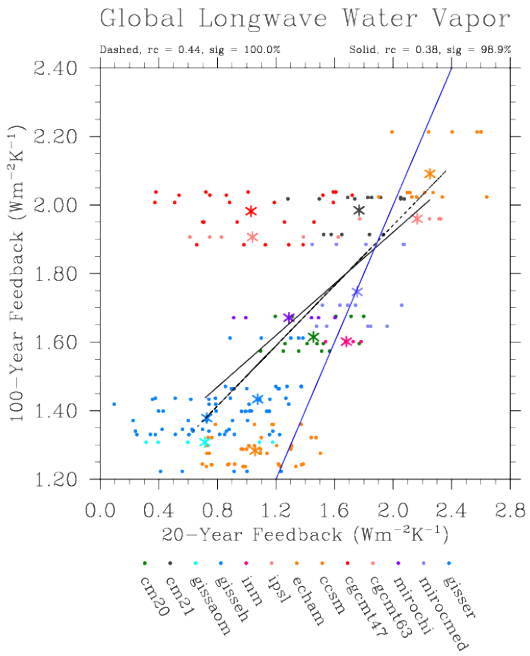

Figure 5.32: 20-year global feedbacks compared with 100-year global feedbacks for LW water vapor as calculated with the RKT and Gregory et al. (2004) method.

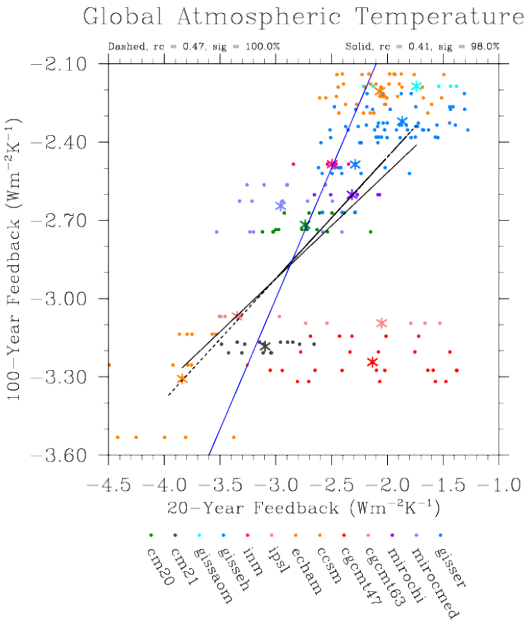

Figure 5.33: 20-year global feedbacks compared with 100-year global feedbacks for atmospheric temperature as calculated with the RKT and Gregory et al. (2004) method.

Chapter 6

Discussion

The ultimate goal of exploring radiative feedback variability between time scales is to find a short-term to long-term link supported by the climate model data of the 20^{th} century. Ideally, if a strong, consistent relationship exists between variability in TOA flux anomalies derived from short and long time periods in models, the short-term variability can then be compared against variability over the same short time scale in observations (or reanalysis data in this case), which could then provide a constraint on the modeled long-term variability. In other words, a one hundred year linear trend can be narrowed down such that the maximum and minimum long-term trend allowed by the constraint of the short-term observations can be extended from the current observations to project and constrain a future state. The work of this thesis motivates this goal by presenting results indicating for which time scales (Section 6.1), variables (Section 6.2), and regions (Section 6.3) long-term constraint by observations might be possible. Through comparing reanalysis observations with models, this work also presents findings on models that consistently behave differently than most models (Section 6.4). Section 6.5 summarizes several feedback estimates and compares results with previous studies. Finally, Section 6.6 briefly discusses ideas for future work.

6.1 Time Scales

This thesis explores the relationship between short-term and long-term feedbacks and feedback variability by comparing 20-year and 100-year characteristics of variability in TOA flux anomalies due to atmospheric temperature, water vapor and surface albedo variability. Variability is characterized over annual, interannual, and decadal time scales. The most desirable short-term measure of variability would be one that

does not change very much depending on which 20-year period is used because then one 20-year period of observations would be sufficient.

In this study, the spread in the 20-year seasonal cycle amplitudes for each model is small compared to that of 20-year trends and 20-year standard deviations. The spread for each model is defined as a percentage of the standard deviation of the 20-year points over the average of the 20-year points for each model. The spread is then presented as the ensemble average. For seasonal amplitude, the spread is about 1%. Also, the annual cycles of models differ more between models than within a single model. Because of the small spread in 20-year seasonal amplitude, we might have more confidence in any relationship found with 100-year trends and feedbacks. However, most of the relationships found between 20-year seasonal amplitudes and 100-year trends and feedbacks depend on the inclusion of a few models that behave differently from the rest. Since models have seasonal amplitudes distinct from one another, this is something that can easily be compared with observations. But, this doesn't necessarily mean that the long-term feedback predicted by the best performing model in terms of seasonal amplitude would be correct.

The spread in the 20-year standard deviation is larger than the spread in seasonal amplitude. The spread is close to 10%. This means that one 20-year period of observations may not be as good a representation of the 100-year standard deviation. The 20-year standard deviation underestimates the 100-year standard deviation because one 20-year period doesn't capture all the extremes and low frequency cycles of the longer period. The spread of the 20-year trends is even larger ($\approx$100%) making its use to estimate 100-year feedbacks more uncertain.

For all variables, 20-year trends were related to 100-year trends with a regression slope of slightly less than one-to-one, but the 20-year trends (when linearly extrapolated to 100-years) were generally larger than the 100-year trends. This is because the y-intercept is not zero for this regression. The discrepancy between the 20-year and 100-year trends is most likely due to a combination of the non-linear behavior of the 100-year time series and the way in which the 20-year segments were separated and analyzed within each segment. The relationship was closest to one-to-one for surface albedo, but the spread in the 20-year trends was also quite large. The spread in the 20-year trends does not come from just a few outliers, but rather from natural variability inherent in the record. Because climate change in these models is not a constant linear change through the 100 years, sampling just 20-years could capture

a much larger or smaller trend than the overall 100-year trend leading to the large spread. Some models show a steady or slow increase in temperature at the beginning of the record and a much steeper temperature increase toward the end of the record indicating a blend of natural variability and climate change in the 20^{th} century simulations. It is also important to note that the spread of 20-year trends is model dependent. For an individual ensemble member, the spread in 20-year trends will differ among models. Models with multiple ensemble members will contribute to the total spread in 20-year trends because there is also some natural variability in the 20-year trend for a particular period across all ensemble members of one model.

While the general relationship between 20-year trends and 100-year trends is positive and almost one-to-one, there are some individual 20-year periods that are of opposite sign to the general trend: a negative 20-year trend corresponding to a positive 100-year trend. This means that 20 years might not be long enough to infer anything about the longer time period of which a particular 20-year period is a part, especially if the long-term trend is very non-linear. To explore this question further using this framework, one would need to repeat the analysis testing different lengths of time over which to average, like 10 years, 25 years, or 30 years. One would (hopefully) be able to see if the relationship between short-term trends and long-term trends becomes stronger as the short-term record is lengthened and to then determine what length of record gives a confident estimate of the longer period trend. Another approach would be to use the same 20-year period across all models and ensemble members and explore how much information about the 100-year trend one particular 20-year period might contain. Using an ensemble of 20-year trends from just one common period across all ensemble members and models would help determine the 20-year trend variability since the same 20-year period should have about the same corresponding long-term trends. The length of the short-term period could be varied as well as the long-term period about which information is desired. The particular time bounds of the specific short-term period length could also be varied. This would hopefully result in a more comprehensive picture of the time lengths in which information about a 'long' record might be contained in a 'short' record.

6.2 Feedback Variables

The 100-year feedbacks are calculated in this methodology as the trend in TOA flux anomalies due to water vapor, atmospheric temperature, and surface albedo

normalized by the linear trend in surface air temperature anomalies. Normalizing by the surface air temperature trend allows comparison between variables. Using 'method 1' trend calculation, the ensemble average longwave water vapor feedback is $1.83 Wm^{-2}K^{-1}$ with a range in the 13 models from 1.42 to 2.45. For atmospheric temperature, the mean and range is -2.73 (-1.98 to -3.51) $Wm^{-2}K^{-1}$; for surface albedo, 0.18 (-0.09 to 0.52) $Wm^{-2}K^{-1}$. The feedbacks calculated with 'method 2' are within a few hundredths of the 'method 1' values. The feedbacks calculated using the Gregory et al. (2004) method are a couple tenths smaller in magnitude for water vapor and within a few hundredths for the other variables, and the ranges are all contained within the previous ranges. The longwave water vapor feedback is largest positive feedback and is canceled by the negative atmospheric temperature feedback. There is close coupling between the water vapor and temperature feedbacks because of the dependence of saturation specific humidity on the temperature according to the Clausius-Clapeyron relationship. The surface albedo feedback is positive on average (although a few ensemble members have a negative feedback) and smaller in magnitude compared with the water vapor feedback. The surface albedo feedback operates at a longer time scale than water vapor. Water vapor responds to warming much quicker than snow or sea ice melts.

6.3 Regions

Seasonality is more pronounced in the northern hemisphere than in the southern hemisphere and thus the northern hemisphere tends to dominate the global seasonal cycle of all three variables. As Colman (2003b), Hall and Qu (2006), and Taylor et al. (2011) point out, the northern hemisphere seasonality contributes most to long-term feedbacks. However, in this study, there tended to be stronger relationships between time scales in the southern hemisphere rather than in the northern hemisphere or globally for surface albedo. That is, the southern hemisphere interannual variability tended to be slightly more related to the southern hemisphere trend than likewise in the NH or globally.

Why would southern hemisphere interannual variability in albedo TOA flux anomalies be more related to long-term trends than globally or in the northern hemisphere? One reason the SH variability might be more related to the SH trend than NH or global variability is to their corresponding trends is that a single process is dominating surface albedo changes in the SH while competing processes are affecting changes in

the NH. For example, the SH surface albedo changes are likely dominated by sea ice changes whereas in the NH, sea ice changes and snow cover changes occur at slightly different times, and the interannual variability for each process might be unrelated or out of phase. Performing this analysis on narrower latitude regions might help isolate reasons for this apparent relationship. Perhaps repeating this analysis for high latitude regions (60°N to 90°N) could isolate interannual variability due to sea ice changes. Mid-latitude region from 30°N to 60°N could isolate interannual variability due to snow cover changes.

While the NH has stronger seasonality in water vapor, the SH has a stronger relationship between 20-year seasonal amplitude and 100-year trend. The temperature annual cycle is larger in the NH, due to more land area, so that seasonal cycle is propagated to the water vapor seasonal cycle because warmer temperatures allow the atmosphere to hold more water vapor. The SH seasonal amplitude is more related to SH trend than the NH or global amplitudes are to their corresponding trends. This could be because the NH has more land area complicating the relationship with a long-term trend. Also, because the global seasonal cycle reflects the cancellation between the NH and SH, a relationship with trends becomes more complicated.

6.4 Models

Thirteen global climate models are used, but not all 13 models are independent. There are probably only about 4 or 5 originally independent models from which all subsequent models were developed. (Knutti, 2010). Some models are even more closely related, such as CGCMT63 and CGCMT47, which differ only in resolution as do MIROCHI and MIROCMED. CM20 and CM21 are different versions of the same model where as GISSEH and GISSER have different ocean models. The linear regression technique assumes that all points are independent. This is technically not the case here; however, the literature is full of studies that use the model ensemble approach to study and interpret ranges of feedback estimates (e.g. Colman, 2003a; Soden and Held, 2006). Adding more models to an analysis doesn't necessarily increase the certainty of the result, but on the other hand including even one 'bad' model can decrease the uncertainty (Knutti, 2010). As suggested by Knutti (2010), if we think of each ensemble member of each model as a possible trajectory of the actual Earth's climate, we can consider these ensemble members to be independent. Further study into how the results might be altered depending on how many and which particular

models are included is an interesting question that is not quantitatively addressed in this thesis.

Upon examining the figures, it appears that the inclusion of certain models sometimes results in a significant relationship while other times the exclusion of those models results in a significant relationship. We wouldn't want to exclude a model just because its behavior is different from the rest of the models if still physically reasonable (Knutti, 2010). For example, for surface albedo, it appears that one model (with two resolutions) in particular behaves differently from the rest of the models: CGCMT47 and CGCMT63. For starters, this model has a negative feedback calculated with the Gregory et al. (2004) method while all other models have a positive feedback. These two models have larger 100-year trends for water vapor and atmospheric temperature. While these two models seem to stand out among the rest of the models, there are examples where these models fall within the pack of models; SH surface albedo trends and surface albedo seasonal cycle amplitude, for example.

6.5 Comparison with previous results

It is also an interesting result if there isn't a relationship where we thought there should be one, because then we can conclude that 20 years is not a sufficient record to see a relationship or the processes involved on short time scales behave differently on long time scales. Taking surface albedo for example, snow melts seasonally and glaciers melt over decades of climate change. Hall and Qu (2006) found a relationship between the northern hemisphere percent seasonal change in snow albedo normalized by the surface temperature change and the 2200-2000 difference in NH albedo normalized by temperature change. However, we don't find a significant relationship between the northern hemisphere normalized seasonal albedo change and the normalized 100-year trend in NH TOA flux anomalies due to surface albedo. Figure 5.18 does show that there is a general relationship of larger amplitude to larger trend. This is consistent with Hall and Qu's work. But, this analysis does not find a significant relationship on these time scales. It appears that by excluding CGCMT47 and CGCMT63 in the regression in Figure 5.18, we might get a completely different regression coefficient. It is also important to note that Hall and Qu (2006) used only 'snow' points over land whereas this thesis analysis includes all land and ocean points in the NH, including sea ice. Also, the long-term temperature change calculated in

Hall and Qu's (2006) study is larger than that calculated in this study so we may not be seeing a large enough signal.

The global 20^{th} century feedbacks calculated in this research are similar to, but slightly smaller than the 21^{st} century feedbacks from the IPCC. The external radiative forcing and climate response over the 20^{th} century is much smaller than over the 21^{st} century which could explain the smaller values. Feedbacks over the 20^{th} century are 1.83 (1.42 to 2.45) $Wm^{-2}K^{-1}$ for LW water vapor, -2.73 (-1.98 to -3.51) $Wm^{-2}K^{-1}$ for atmospheric temperature, and 0.18 (-0.09 to 0.52) $Wm^{-2}K^{-1}$ for surface albedo. The 20^{th} century contains natural climate variability in addition to a small climate change signal. Comparing these values with the feedbacks calculated from an unforced, natural variability simulation by one climate model (Colman and Power, 2010), would be useful. The climate model used in Colman and Power (2010) is not included in this work. Colman and Power (2010) find that the water vapor feedback in unforced simulations is about two-thirds that of the forced case. The smallest LW water vapor feedback calculated over the 20^{th} century is roughly three-fourths that of the 21st century. Colman and Power (2010) also find a near-zero lapse rate feedback and some models in this study have atmospheric temperature feedbacks that suggest near-zero lapse rate feedbacks, assuming a reasonable value for the Planck feedback of about -3.2 $Wm^{-2}K^{-1}$ (Soden and Held, 2006). Colman and Power (2010) find a stronger surface albedo feedback in unforced simulations than in forced simulations, and some models in this study have larger surface albedo feedbacks than the 21^{st} century feedbacks given by the IPCC.

6.6 Future Work

The range of feedback estimates using reanalysis observations and 20-year to 100-year relationships depend on several factors. One is the selection of models used in the analysis. Many of the relationships between a 20-year feedback variability metric and the 100-year feedback were dependent on the inclusion of a few particular models. Other relationship may be strengthened by the exclusion of the same models. Future work exploring the dependence of these results on model inclusion would be an interesting extension, as well as including more of the IPCC models to the analysis. Feedback estimates may also depend on the time scale metrics used and the time period lengths used. Another interesting expansion of this research would be to explore the dependence of any of the relationships on the time periods used to

compute the metrics. For example, one could test how these results would be altered by using a short-term period of 30 years instead of 20 years. One might also select different definitions of feedback variability metrics to compute and compare.

Chapter 7

Conclusion

The climate is warming. It is of scientific and societal interest to know how much the climate will warm in the future. The amount of warming depends partly on the climate sensitivity of the Earth, that is, for a given radiative perturbation that forces the climate system out of equilibrium, by how much will the climate warm until reaching a new balance in the Earth's radiative energy balance. The climate sensitivity can be separated into components of internally driven processes that act to either amplify or dampen the initial response of the climate to an external radiative forcing. These internal processes are radiative feedbacks. Scientists use global climate models to learn about climate sensitivity and feedbacks. The current suite of atmospheric global climate models coupled to slab ocean models calculate climate sensitivity values of 2.1 to 4.4 Kelvin. This spread in the estimated climate sensitivity is due in part to the uncertainties of the individual climate feedbacks including: water vapor with a mean and range of $1.8 \pm 0.18 Wm^{-2}K^{-1}$, lapse rate with a mean and range of $-0.84 \pm 0.26 Wm^{-2}K^{-1}$ and corresponding atmospheric temperature feedback of $-3.2 \pm 0.3 Wm^{-2}K^{-1}$, surface albedo with a mean and range of $0.26 \pm 0.08 Wm^{-2}K^{-1}$, and clouds with a mean and range of $0.69 \pm 0.38 Wm^{-2}K^{-1}$ (Randall et al., 2007). While the cloud feedback contributes most to the uncertainty in the climate sensitivity, the uncertainty in the water vapor, lapse rate (related to atmospheric temperature), and surface albedo feedbacks also contribute. Using observationally derived estimates of climate sensitivity and feedbacks is one way in which to attempt to constrain the climate sensitivity estimates from models. Because only a few decades of radiation observations from satellites exist, climate sensitivity and feedbacks inferred from this short record can most confidently be used to constrain modeled climate sensitivity and feedback estimates using the same time period. If the goal is to constrain the estimates of climate sensitivity and feedbacks over the long-term (century scale),

there must be a relationship between modeled climate sensitivity and feedbacks estimated from a short record and those estimated using a longer record. To establish a foundation to be able to address the question of constraining climate sensitivity and feedbacks using observations, this thesis characterizes the short-term and long-term feedback variability using climate model data.

7.1 Does the short-term variability in TOA flux anomalies tell us anything about future trends in models?

The radiative kernel technique was used to calculate TOA flux anomalies and radiative feedbacks due to water vapor, atmospheric temperature, and surface albedo over the 20^{th} century as simulated by the current suite of coupled atmosphere-ocean global climate models. Feedbacks of the 20^{th} century were computed in two ways: using the full 100 years and using five sequential, non-overlapping 20-year periods within the 20^{th} century. First, metrics of feedback variability from the short-term (collective 20-year segments) were regressed onto metrics of feedback variability from the long-term (entire 20^{th} century). Relationships between the amplitude of the seasonal cycle of feedback variables and the 100-year trend in TOA flux anomalies due to feedback variables were quantified (Results, Section 5.6); as were relationships between feedbacks calculated over interannual variability and 100-year trends in TOA flux anomalies (Results, Section 5.5).

Did we find any significant relationships between a short-term metric of feedback variability and a long-term metrics of feedback variability? We find a significant relationship between the 20-year annual time scale metric and the 100-year feedbacks for water vapor and atmospheric temperature in the northern and southern hemispheres. We don't find this relationship for surface albedo. While large 20-year interannual metrics relate to large 100-year feedbacks, we do not find a significant relationship between surface albedo metrics for any variable or region. With relationships (to varying degrees of significance) between short-term and long-term feedback variability, we then characterized short-term feedback variability from an observational dataset to compare with modeled short-term feedback variability, especially for the 20-year annual cycle amplitude.

7.2 Can climate sensitivity components be constrained by observations through this method of analysis?

We computed TOA flux anomalies and feedbacks from twenty years of the ECMWF ERA-Interim observational reanalysis product. Using the seasonal amplitude of feedback variables and interannual feedbacks calculated from the reanalysis data, a constraint on 100-year trends in TOA flux anomalies normalized by surface air temperature anomalies (i.e. feedbacks) was estimated using any 'short-term' to 'long-term' relationship established from the model data. These estimates of long-term feedbacks were compared with other previous feedback estimates.

The reanalysis provided a constraint on the 20-year interannual metric that corresponded to a range in the estimated 100-year feedback that was smaller than the range of modeled atmospheric temperature and water vapor feedbacks that fell within the range of reanalysis 20-year observations. Because the 20-year interannual metric is not significantly related to the 100-year feedback, we cannot determine a constraint using this methodology. For the 20-year annual cycle amplitude, only a few models fell within the range of the reanalysis values. The corresponding estimates of 100-year feedbacks were close to the total range of modeled 100-year feedbacks.

However, even if the estimated feedback ranges are smaller than existing ranges, we assume in this analysis that the observational values are perfect. Including an error estimate in the reanalysis observations may expand our estimated range to be consistent or larger than existing ranges. This suggests that these results are at least consistent with existing ranges or suggest that this may not be a very fruitful method in which to constrain estimates of long-term feedbacks and climate sensitivity, at least until GCMs show better agreement or until we can objectively determine which models to use in this type of analysis. While these results may depend on several factors including selection of models included in the analysis, reliability of observational product, and time scale metrics and time periods used, this research does suggest that long-term feedbacks may be better constrained by the annual cycle than interannual variability.

BIBLIOGRAPHY

Bony, S., and Coauthors, 2006: How well do we understand and evaluate climate change feedback processes? *Journal of Climate*, **19**, 3445-3482.

Chung, E., B. J. Soden, and B. Sohn, 2010: Revisiting the determination of climate sensitivity from relationships between surface temperature and radiative fluxes. *Geophysical Research Letters*, **37**, L10703, doi:10.1029/2010GL043051.

Colman, R. A., and S. B. Power, 2010: Atmospheric radiative feedbacks associated with transient climate change and climate variability. *Climate Dynamics*, **34**, 919-933.

Colman, R. A., 2003a: A comparison of climate feedbacks in general circulation models. *Climate Dynamics*, **20**, 865-873.

Colman, R., 2003b: Seasonal contributions to climate feedbacks. *Climate Dynamics*, **20**, 825-841.

Dee, D. P. and Coauthors, 2011: The ERA-Interim reanalysis: Configuration and performance of the data assimilation system. *Q. J. R. Meteorol. Soc.*, **137**, 553-597. (ECMWF ERA-Interim data used in this research have been provided by ECMWF).

Dessler, A. E., 2010: A determination of the cloud feedback from climate variations over the past decade. *Science*, **330**, 1523-1527.

Dessler, A. E. and S. Wong, 2009: Estimates of the water vapor climate feedback during El Niño-Southern Oscillation. *Journal of Climate*, **22**, 6404-6412.

Dessler, A. E., Z. Zhang, and P. Yang, 2008: Water-vapor climate feedback inferred from climate fluctuations, 2003-2008. *Geophysical Research Letters*, **35**, L20704, doi:10.1029/2008GL035333.

Flanner, M. G., K. M. Shell, M. Barlage, D. K. Perovich, and M. A. Tschudi, 2011: Radiative forcing and albedo feedback from the northern hemisphere cryosphere between 1979 and 2008. *Nature Geoscience*, **4**, 151-155.

Forster, P. M. and J. M. Gregory, 2006: The climate sensitivity and its components diagnosed from earth radiation budget data. *Journal of Climate*, **19**, 39-52.

Gregory, J. M., and Coauthors, 2004: A new method for diagnosing radiative forcing and climate sensitivity. *Geophysical Research Letters*, **31**, L03205, doi:10.1029/2003GL018747.

Hall, A., and X. Qu, 2006: Using the current seasonal cycle to constrain snow albedo feedback in future climate change. *Geophysical Research Letters*, **33**, L03502, doi:10.1029/2005GL025127.

Hansen, J., and Coauthors, 2005: Earth's energy imbalance: confirmation and implications. *Science*, **308**, 1431-1435.

Harries, J. E., and C. Belotti, 2010: On the Variability of the Global Net Radiative Energy Balance of the Nonequilibrium Earth. *Journal of Climate*, **23**, 1277-1290.

IPCC, 2007: Summary for Policymakers. In: *Climate Change 2007: The Physical Science Basis. Contribution of Working Group I to the Fourth Assessment Report of the Intergovernmental Panel on Climate Change.* [Soloman, S., D. Qin, M. Manning, Z. Chen, M. Marquis, K. B. Averyt, M. Tignor, and H. L. Miller (eds.)]. Cambridge University Press, Cambridge, United Kingdom and New York, NY, USA.

Jonko, A. K., K. M. Shell, B. M. Sanderson, and G. Danabasoglu, 2011: Estimating radiative climate feedbacks in GCM simulations with large CO2 forcing. *Journal of Climate*, in revision.

Kiehl, J. T. 2007: Twentieth century climate model response and climate sensitivity. *Geophysical Research Letters*, **34**, L22710, doi:10.1029/2007GL031383.

Knutti, R., 2010: The end of model democracy? An editorial comment. *Climatic Change*, **102**, 395-404.

Knutti, R., G. A. Meehl, M. R. Allen, and D. A. Stainforth, 2006: Constraining climate sensitivity from the seasonal cycle in surface temperature. *Journal of Climate*, **19**, 4224-4233.

Lin, B., Q. Min, W. Sun, Y. Hu, and T. Fan, 2011: Can climate sensitivity be estimated from short-term relationships of top-of-atmosphere net radiation and surface temperature? *Journal of Quantitative Spectroscopy & Radiative Transfer*, **112**, 177-181.

Randall, D. A. and Coauthors, (2007): Climate models and their evaluation. In: *Climate Change 2007: The Physical Science Basis. Contributions of Working Group I to the Fourth Assessment Report of the Intergovernmental Panel on Climate Change*. Edited by S. Solomon et al., pp. 591-662, Cambridge Univ. Press, Cambridge, U.K.

Roe, G., 2009: Feedbacks, timescales, and seeing red. *Annual Review of Earth and Planetary Sciences*, **37**, 93-115.

Shell, K., J. Kiehl, and C. Shields, 2008: Using the radiative kernel technique to calculate climate feedbacks in NCAR's Community Atmospheric Model. *Journal of Climate*, **21**, 2269-2282.

Slingo, A., J. A. Pamment, R. P. Allan, and P. S. Wilson, 2000: Water vapor feedbacks in the ECMWF Reanalyses and Hadley Centre Climate Model. *Journal of Climate*, **13**, 3080-3098.

Soden, B. J., I. M. Held, R. A. Colman, K. M. Shell, J. T. Kiehl, and C. A. Shields, 2008: Quantifying climate feedbacks using radiative kernels. *Journal of Climate*, **21**, 3504-3520.

Soden, B. J., and I. M. Held, 2006: An assessment of climate feedbacks in coupled ocean-atmosphere models. *Journal of Climate*, **19**, 3354-3360.

Solomon, S., D. Qin, M. Manning, R.B. Alley, T. Berntsen, N.L. Bindoff, Z. Chen, A. Chidthaisong, J.M. Gregory, G.C. Hegerl, M. Heimann, B. Hewitson, B.J. Hoskins, F. Joos, J. Jouzel, V. Kattsov, U. Lohmann, T. Matsuno, M. Molina, N. Nicholls, J. Overpeck, G. Raga, V. Ramaswamy, J. Ren, M. Rusticucci, R. Somerville, T.F. Stocker, P. Whetton, R.A. Wood and D. Wratt, 2007: Technical Summary. In: *Climate Change 2007: The Physical Science Basis. Contribution of Working Group I to the Fourth Assessment Report of the Intergovernmental Panel on Climate Change*. [Solomon, S., D. Qin, M. Manning, Z. Chen, M. Marquis, K.B. Averyt, M. Tignor and H.L. Miller (eds.)]. Cambridge University Press, Cambridge, United Kingdom and New York, NY, USA.

Taylor, P. C., R. G. Ellingson, and M. Cai, 2011: Seasonal variations of climate feedbacks in the NCAR CCSM3. *Journal of Climate*, **24**, 3433-3444.

Trenberth, K. E., J. T. Fasullo, C. O'Dell, and T. Wong, 2010: Relationships between tropical sea surface temperatures and top-of-atmosphere radiation. *Geophysical Research Letters*, **37**, L03702, doi:10.1029/2009GL042314.

Trenberth, K. E., J. T. Fasullo, and J. Kiehl, 2009: Earth's global energy budget. *Bulletin of the American Meteorological Society* **90**, 311-323.

Wetherald, R. T., and S. Manabe, 1988: Cloud feedback processes in a general circulation model. *Journal of Atmospheric Science*, **45**, 1397-1416.

Wielicki, B. A., and Coauthors, 2002: Evidence for large decadal variability in the tropical mean radiative energy budget. *Science*, **295**, 841-844.

Wong, T., B. A. Wielicki, R. B. Lee III, G. L. Smith, K. A. Bush, and J. K., Willis, 2006: Reexamination of the observed decadal variability of the earth radiation budget using altitude-corrected ERBE/ERBS nonscanner WFOV data. *Journal of Climate*, **19**, 4028-4040.